GLYoxal Retrievals from TROPOMI (GLYRETRO)

Sentinel-5p + Innovation - Theme 1: CHOCHO

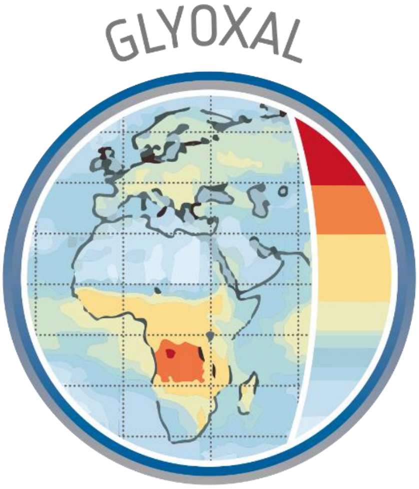

Algorithm Theoretical Baseline Document

document number	:	S5p+I_CHOCHO_BIRA_ATBD
authors	:	Christophe Lerot, Trissevgeni Stavrakou, Michel Van Roozendael, Leonardo M.A. Alvarado, Andreas Richter
Distributed to	:	Christian Retscher, Marie-Helene Rio, Stefano Casadio, Daniele Gasbarra
issue	:	3.1
date	:	2021-12-22
status	:	Final

Contents

List of Figures

List of Tables

1 Introduction

1.1 Purpose and objective

The present document is the Algorithm Theoretical Basis Document (ATBD) describing the BIRA-IASB scientific algorithm to retrieve glyoxal tropospheric vertical columns from the S5p/TROPOMI measurements.

The purpose of the document is to give detailed mathematical description of the algorithm and to discuss the necessary input and auxiliary data, and the output that will be generated. In addition, information about the expected size of the product, expected calculation times, and the expected accuracy are provided.

1.2 Document overview

Section 1 and 2 provide the introduction and references. Section 3 lists the acronyms, terms and definitions used in this document. Section 4 gives an overview of the instrument. Section 5 describes the context of the algorithm, a general overview, heritage from other missions or projects, as well as current defined product requirements. Section 6 specifies the algorithm including a high-level block diagram and details about each main component, including error estimates. Section 7 discusses the feasibility of the algorithm as a L2 processor and section 8 gives a description how the algorithm can be validated.

2 Applicable and Reference Documents

2.1 Applicable Documents

[AD01] Sentinel-5p Innovation (S5p+I) - Statement of Work - EOP-SD-SOW-2018-049,
source: ESA, **issue:** 2, **date**: 20/08/2018.

[AD02] Sentinel-5p+Innovation: Theme 1; Glyoxal Retrievals from TROPOMI (GLYRETRO): Requirement Baseline Document,
source: BIRA-IASB, **issue**: 2.0, **ref**: S5p+I_CHOCHO_BIRA_RB, **date:** 2019-11-01.

[AD03] Sentinel-5p+Innovation: Theme 1; Glyoxal Retrievals from TROPOMI (GLYRETRO): Auxiliary User Manual,
Source: BIRA-IASB, **issue:** 2.0, **ref:** S5p+I_CHOCHO_BIRA_AUM, **date:** 2021-10-19.

[AD04] Sentinel-5p+Innovation: Theme 1; Glyoxal Retrievals from TROPOMI (GLYRETRO): Product Validation Report,
Source: IUP-Bremen, **issue:** 2.1, **ref:** S5p+I_CHOCHO_BIRA_VR, **date:** 2021-12-22.

[AD05] Sentinel-5p+Innovation: Theme 1; Glyoxal Retrievals from TROPOMI (GLYRETRO): Product User Manual Report,
Source: BIRA-IASB, **issue:** 1.1, **ref:** S5p+I_CHOCHO_BIRA_PUM, **date:** 2021-12-22.

2.2 Reference Documents

[RD01] Terms, and symbols in the TROPOMI Algorithm Team;
source: KNMI; **ref**: SN-TROPOMI-KNMI-L2-049-MA; **issue**: 1.0.0; **date**: 2015-07-16

[RD02] TROPOMI Instrument and Performance Overview.
source:KNMI;ref:S5P-KNMI-L2-0010-RP; **issue**:0.10.0; **date**:2014-03-15.

[RD03] Sentinel-4 Level-2 Geophysical Algorithm Development Plan, RAL, S4-L2-RAL-GADP-2001, Issue 1.2, 2016.

[RD04] Sentinel-5 Level-2 Prototype Processor Development Requirements Specification;
source: ESA; **ref**: S5-RS-ESA-GR-0131; **issue**: 1.7; **date**: 2018-06-29.

[RD05] Copernicus Sentinels 4 and 5 Mission Requirements Traceability Document (MRTD):
source: ESA; **ref**: EOP-SM/2413/BV-bv; **issue**: 2.0 **date**: 2017-07-07.

[RD06] Sentinel-4 L2 Processor Component Development–Project Management Plan, DLR, S4-L2-DLR-PMP-1004, issue 2.1, 2017-05-31.

[RD07] S5L2PP: Record of agreements from negotiation;
source: S5L2PP proposal consortium; **ref**: ST-ESA-S5L2PP-NOT-003; **Issue**: 1.1; **date**: 2016-09-02.

[RD08] Preparing elevation data for Sentinel 5 precursor.
source: KNMI, **ref**: S5P-KNMI-L2-0121-TN, **Issue**: 2.0.0, **date**: 2015-09-11.

[RD09] S5P/TROPOMI ATBD of the total and tropospheric NO2 data products;
source: KNMI; **ref**: S5P-KNMI-L2-0005-RP; **issue**: 1.4.0; **date**: 2019-02-06.

[RD10] CAMS Forecast Data Needs for Sentinel-4 and -5 Data Processing, edited by B. Veihelmann,
Issue: 0.6, **date:** 15/06/2018.

[RD11] Sentinel-4 Geophysical Algorithm Verification Report 2; Thomas Wagner, Janis Pukite
Source: MPIC; **ref:** S4-L2-MPIC-GAVR-3003; **issue:** 2.3; **date:** 2020-08-24.

2.3 Electronic references

[URL01] http://uv-vis.aeronomie.be/software/QDOAS/

[URL02] http://www.rtslidort.com/

[URL03] SPEC CPU2006 Results; **url:** https://www.spec.org/cpu2006/results/

3 Acronyms, Terms and Definitions

Terms, definitions and abbreviated terms that are used in development program for the TROPOMI L2 data processors are listed in [RD01].

The most important symbols and acronyms related to the data product described in this document are the following:

A	averaging kernel
m	altitude-resolved air mass factor or weighting function
M	air-mass factor
N_s	slant column density
N_v	vertical column density

Acronym	Explanation
AAI	Absorbing Aerosol Index
AMF	Air Mass Factor
ATBD	Algorithm Theoretical Basis Document
BIRA-IASB	Royal Belgian Institute for Space Aeronomy
BOA	Bottom of Atmosphere
CAMS	Copernicus Atmosphere Monitoring Service
CF	Climate and Forecast metadata conventions
CHOCHO	Glyoxal
CRB	Cloud as Reflecting Boundaries
CTM	Chemistry Transport Model
DOAS	Differential Optical Absorption Spectroscopy
ESA	European Space Agency
FRESCO	Fast Retrieval Scheme for Clouds from the Oxygen A band
GsCOS	Global Climate Observing System
HCHO	Formaldehyde
NMVOC	Non-Methane Volatile Organic Compound
OMI	Ozone Monitoring Instrument
SCD	Slant Column Density
SO_2	Sulphur Dioxide
SZA	Solar Zenith Angle
TROPOMI	Tropospheric Monitoring Instrument
VAA	Viewing Azimuth Angle
VCD	Vertical Column Density
VOC	Volatile Organic Compound
VZA	Viewing Zenith Angle

4 TROPOMI instrument description

A description of the TROPOMI instrument and performance, referred to from all ATBDs, can be found in [RD02]. See also the overview paper of Veefkind et al. (2012).

5 Introduction to the glyoxal product

5.1 Background

Satellite observations of NMVOCs are essential to support air quality and chemistry-climate related studies from the regional to the global scale. Information on their atmospheric concentrations can be derived using remote sensing techniques for a limited number of species, including formaldehyde (HCHO) and glyoxal (CHOCHO). Glyoxal is mostly produced in the atmosphere as an intermediate product in the oxidation of other non-methane VOCs. It is also directly emitted from fire events and combustion processes. Several attempts to establish a glyoxal global budget using chemistry transport models (Fu et al., 2008; Myriokefalitakis et al., 2008; Stavrakou et al., 2009) have estimated the production from natural sources and fires to about 70% and from human activities to about 30%. Owing to its short lifetime, elevated glyoxal concentrations are observed near emission sources (Figure 1). Measurements of atmospheric glyoxal concentrations therefore provide quantitative information on the different types of VOC emission and can help to better assess the quality of current inventories (e.g. Li et al., 2016; Liu et al., 2012; Stavrakou et al., 2016). In addition, glyoxal is also known to significantly contribute to the total budget of secondary organic aerosols (Washenfelder et al., 2011), which impact both air quality and climate forcing. A glyoxal signal has also been detected from different platforms over some oceanic regions (Coburn et al., 2014; Lawson et al., 2015; Lerot et al., 2010; Sinreich et al., 2010; Vrekoussis et al., 2009; Wittrock et al., 2006) of which the origin remains unclear. Glyoxal has similar type of sources as formaldehyde, with different production yields. Therefore, the combination of glyoxal and formaldehyde observations provide additional constraints to better discriminate different type of NMVOC sources. The glyoxal/formaldehyde ratio is regularly proposed as a metric for such a speciation (Chan Miller et al., 2016; DiGangi et al., 2012; Kaiser et al., 2015; Vrekoussis et al., 2010).

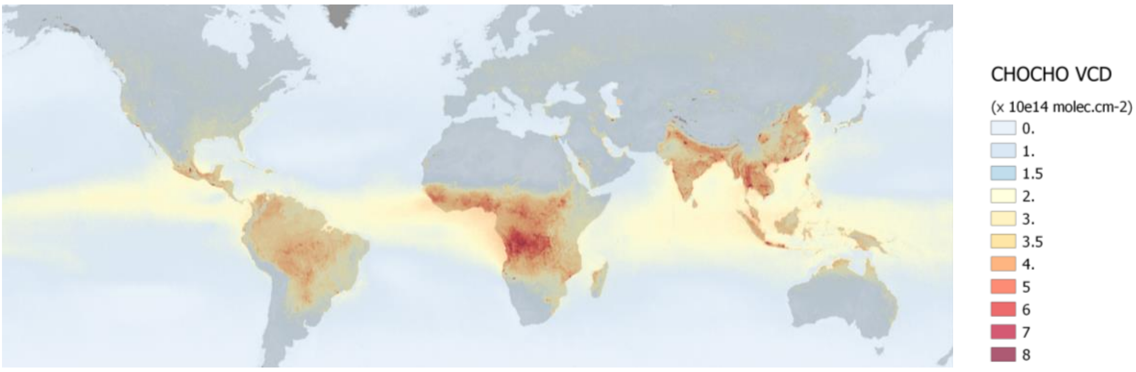

Figure 1: Mean glyoxal tropospheric vertical columns retrieved from three years of TROPOMI observations (2018-2020).

5.2 Heritage

Glyoxal has three weak absorption bands in the visible spectral range, which makes possible the retrieval of its tropospheric columns from spectral radiance measurements. Scientific satellite glyoxal products have been already developed in the past for different instruments. The first glyoxal measurements from space have been proposed by Wittrock et al. (2006) on SCIAMACHY/Envisat observations. Then, measurements from other nadir-viewing instruments have been exploited by different teams to derive information on glyoxal concentrations, from the GOME-2 sensors aboard the Metop platforms (Lerot et al., 2010; Vrekoussis et al., 2009), from OMI aboard Aura (Alvarado et al., 2014; Chan Miller et al., 2014; Wang et al., 2019) and more recently from TROPOMI on S5P (Alvarado et al., 2019). All those different algorithms rely on a similar DOAS approach and most of the differences lie in the choice of the fit settings and of the auxiliary input data.

Until recently, retrievals of glyoxal tropospheric columns were considered as by-products but the potential offered by glyoxal retrievals is more and more recognized. As part of the preparation of the baseline for the future L2 Operational Processors of the Sentinel-4 and -5 missions, glyoxal has therefore been included in the list of the core products [RD03] [RD04]. This is also in this context that glyoxal retrievals are one of the theme covered by the S5P+Innovation initiative, aiming at further exploiting the capability of the TROPOMI instrument [AD01]. The exploitation of the S5p spectra to retrieve glyoxal VCDs offers the potential to have an unprecedented view of the spatiotemporal variability of NMVOC emissions, thanks to the high signal-to-noise ratio of the measurements carried out at very high spatial resolution.

5.3 Requirements

The scientific requirements have been discussed in the requirement baseline document [AD02]. TROPOMI/S5p is, along with the future missions Sentinel-4 and -5, the space component of the European Earth Observation program *Copernicus*. It provides crucial observations for a series of trace gases relevant to air quality and climate change monitoring. General requirements have been defined for such space observations to serve as best as possible those two themes [RD05] and requirements for glyoxal retrievals should be defined in regards to them.

Requirements have been defined for a series of key species, including particulate matter, ozone, NO_2, CO, SO_2 and HCHO. Since it has been generally considered as a second priority, no requirement on the glyoxal column uncertainty has been defined in the S4/5 MRTD [RD05]. For the requirements on horizontal resolution and revisit time, we can use those defined for the formaldehyde columns, as those two species are useful for similar applications. The spatial requirement for HCHO has been set to 5/20 km (goal/threshold) for air quality applications and relaxed to 10/50 km for climate applications. The revisit time requirement is 0.5/2 hours for air quality applications and can obviously not be met for space instruments boarded on LEO platforms such as TROPOMI. On contrary, the future Sentinel-4 instrument aboard a geostationary platform will provide a one-hour revisit time.

Unlike for TROPOMI, glyoxal is part of the initial list of core operational products for Sentinel-4 and -5. In this context, requirements on this product have also been defined [RD04] [RD06] [RD07] and are given in Table 1. While one single total uncertainty requirement is defined for Sentinel-4, two separate values are defined for the random and systematic components of the uncertainty in Sentinel-5. Owing to the faint glyoxal signal, its associated random uncertainty is large on individual measurements, in the range 6-10 x 10^{14} molec.cm^{-2} for TROPOMI (see section 6.5). Thus, it generally meets the random error requirement as defined for Sentinel-5. Estimates of the systematic errors indicate that the S5 systematic error requirement is also met in favorable conditions (clear sky conditions, no aerosol load…). This is further discussed in sections 6.5.4 and 8. The Sentinel-4 requirement combining the two error components is much more difficult to meet on individual measurements. However, the random uncertainty can be reduced by averaging several observations. Provided the threshold requirement of 20 km for the spatial requirement, up to 16 TROPOMI observations may be combined to reduce the random error and thus making the Sentinel-4 requirement reachable as well. In summary, the glyoxal requirements currently defined are realistic and are met for TROPOMI observations under favorable conditions (no contamination by clouds, aerosol or snow/ice).

Table 1 : Uncertainty Requirements on glyoxal column retrievals defined for the Sentinel-4 and -5 missions.

	Uncertainty (Threshold)	**Conditions**
Sentinel-4	7 x 10^{14} molec.cm^{-2} or 50% (least stringent)	SZA < 60° VZA < 60° cloud fraction < 20% VCD > 5 x 10^{14} molec.cm^{-2}
Sentinel-5	Random error: < 1.5 x 10^{15} molec.cm^{-2} Systematic error: < 2.5 x 10^{14} molec.cm^{-2} or 50% (least stringent)	SZA < 70° VZA < 70°

6 Algorithm Description

6.1 Overview

The general method used for the derivation of CHOCHO VCDs from visible spectral measurements is the Differential Optical Absorption Spectroscopy method (DOAS; Platt and Stutz, 2008) which involves two main steps. First, the effective slant column amount (corresponding to the integrated glyoxal concentration along the mean atmospheric optical path: N_s) is derived through a least-squares fit of the measured Earth reflectance spectrum by laboratory absorption cross-sections. Second, slant columns are converted into vertical columns by means of air mass factors (AMF) obtained from suitable radiative transfer calculations, accounting for the surface properties, observation geometry, and best-guess glyoxal vertical profiles. In addition, for weak absorbers such as glyoxal, a background normalization procedure is often applied, which relies on the comparison of measured and modelled slant columns in a reference sector where the glyoxal concentrations are expected to be low.

The sensitivity of space nadir observations to the lowermost atmospheric layers is intrinsically limited because of the combined effect of Rayleigh and Mie scattering that limits the radiation fraction scattered back toward the satellite. Although more limited than in the UV spectral range, this decrease of the sensitivity to the gas concentration in the boundary layer also occurs for species retrieved in the visible spectral range such as glyoxal. Also, typical glyoxal optical depths are very small (one order of magnitude less than other species absorbing in the same spectral range such as NO_2) making glyoxal retrievals noisy and very sensitive to spectral interferences with other species. While the precision (or random uncertainty) is driven by the signal to noise ratio of the recorded spectra and by the width of the retrieval interval, the systematic uncertainty (or trueness) is limited by the current knowledge on the external parameters needed in the different retrieval steps.

The selection of the optimal retrieval interval must maximize the sensitivity of the inversion to the CHOCHO absorption signatures, while minimizing errors from geophysical and instrument related spectral features. The retrieval interval should be chosen as wide as possible to maximize the number of sampling points, while avoiding overlap with strong atmospheric spectral features from interfering species (e.g. NO_2, Ring, O_4, liquid water signature). Systematic errors originating from such spectral interferences are generally reduced for weak absorbers by applying appropriate background corrections on the columns. Also normalizing the recorded Earthshine backscattered spectra by another reference Earthshine spectrum taken in a remote region with expected low glyoxal levels instead of using an irradiance spectrum also contributes to reduce systematic errors due to spectral interferences and/or instrumental limitations (Anand et al., 2015; Schönhardt et al., 2012; De Smedt et al., 2008). However, background correction procedures do not remove entirely systematic errors as they are spatially dependent and may therefore differ from their values within the reference sector. It has also been shown that there are significant interferences between glyoxal and a spectral signature related to the liquid water in remote oceanic regions, leading to strong negative biases in the retrieved glyoxal VCDs if not properly accounted for (Wittrock et al., 2006). For the heritage instrument GOME-2, Lerot et al., (2010) have reduced those spectral interferences by using two successive DOAS fits in different intervals in order to prescribe the liquid water optical depth in the actual glyoxal retrieval. For OMI, other teams have chosen to fit simultaneously glyoxal and liquid water cross-sections in one single fit interval with reasonable performance (Alvarado et al., 2014). Recent reinvestigation of this issue using TROPOMI observations has shown that fitting the liquid water optical depth simultaneously to glyoxal performs well like for OMI.

TROPOMI probes the Earth's atmosphere globally with a very high spatial resolution of about 3.5x7 km^2 (3.5x5.5 km^2 from August 2019 onwards) and has a signal to noise ratio larger than 1500 in the visible spectral range. Although spatial and/or temporal averages is still needed to isolate meaningful typical glyoxal signal, those improved performances allow to maintain a higher level of details in the glyoxal VCDs fields and thus valuable information to better study NMVOC emissions. Requirements in terms of systematic uncertainties as discussed before remain challenging to meet, as glyoxal is very sensitive to spectral interferences with other species. Also a priori knowledge of the glyoxal vertical distribution needed for AMF computation may be quite uncertain and introduce significant systematic errors. In addition, databases of external parameters required in the retrieval algorithm may also be available at a much coarser resolution than that of TROPOMI measurements, introducing also large errors in the final retrieved vertical columns, especially for localized sources (Heckel et al., 2011). This points to the importance to have reliable error estimates as well as averaging kernels along with the retrieved columns.

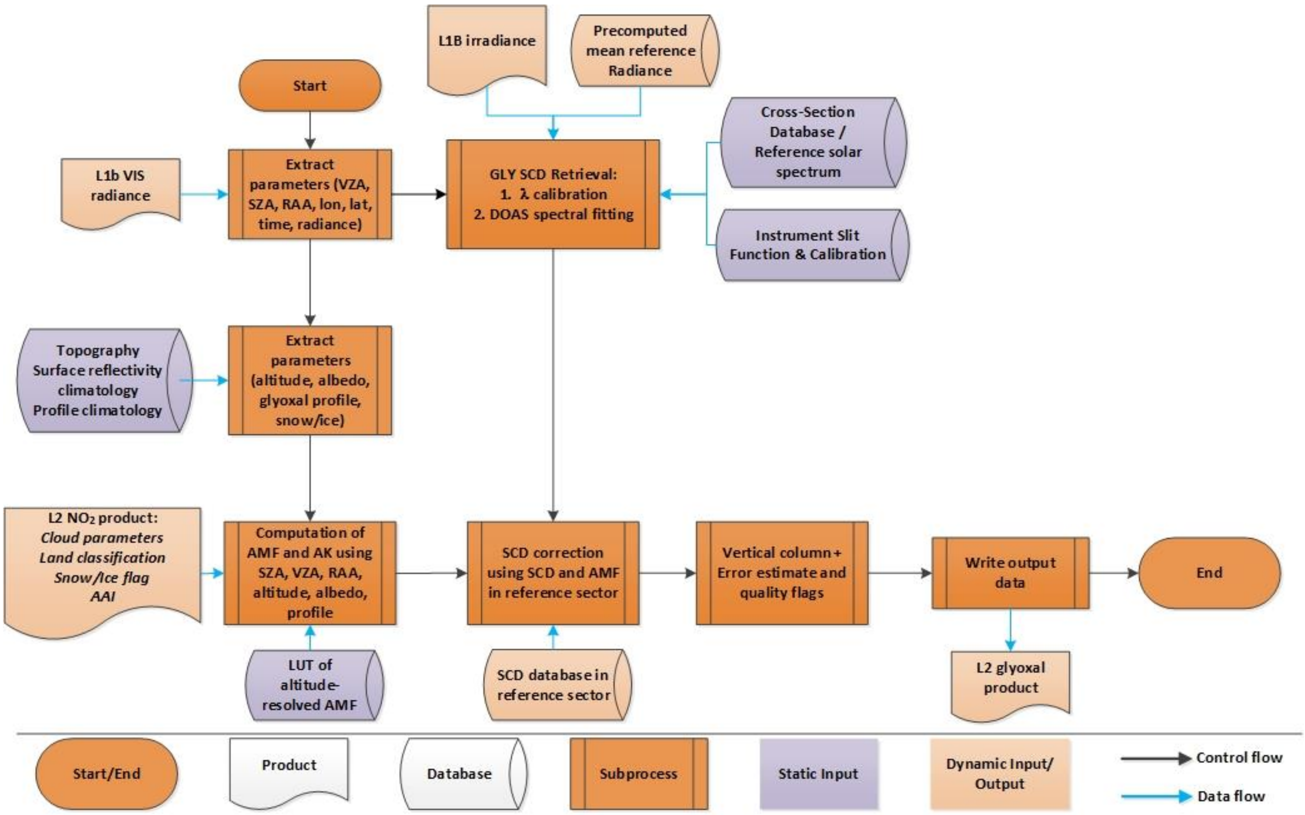

Figure 2: Flow diagram of the CHOCHO retrieval algorithm.

Figure 2 shows the flow diagram of the BIRA-IASB CHOCHO retrieval algorithm. The interdependencies with auxiliary data and other L2 retrievals, such as clouds and aerosols are also represented. This flowchart includes all different steps necessary to the CHOCHO retrieval, i.e. (1) the slant column density derived from the measured reflectance spectrum, (2) the AMF computation for the conversion of the slant column into a vertical column and (3) the background normalization required in the case of weak absorbers such as glyoxal.

The radiance and irradiance data are read from the L1b files, along with geolocation data as pixel coordinates, observation geometry (sun and viewing angles). The relevant absorption cross section data as well as characteristics of the instrument are used as input for the CHOCHO slant column density determination (N_s), which is derived from a DOAS fit performed in an interval from 435 to 460 nm. The DOAS fit also uses as reference mean radiance spectra, which are computed using all observations of the day of interest (see section 6.2.1). Optionally, precomputed mean reference radiance spectra can be provided to the DOAS software. Subsequently, the slant column is converted to a vertical column (N_v) through division by an air mass factor (M) which accounts for the average light path through the atmosphere. For this purpose, several auxiliary data are read from external sources: surface albedo and elevation, and the a priori shape of the vertical glyoxal profile in the atmosphere. The AMF is computed by combining an a priori glyoxal vertical profile shape and altitude-resolved air mass factors extracted from a pre-computed look-up-table. This look up table has been created using the VLIDORTv2.7 radiative transfer model (see Spurr and Christi, 2019) at a single wavelength representative for the retrieval interval (i.e. 448 nm). It is also used to compute the so-called DOAS-type total column averaging kernels (Eskes and Boersma, 2003), which are essential information on the measurement vertical sensitivity and are required for comparison with other types of data (Veefkind et al., 2012). Normalization of the remote background slant column is performed in an additional step. This normalization consists in adding a differential slant column to all retrieved slant columns before their conversion to the vertical column. This differential column is determined on a daily basis and ensures that the mean of the retrieved glyoxal vertical columns in a reference sector (typically the Pacific ocean) is equal to a reference value $N_{v,0,ref}$.

The final CHOCHO vertical column is obtained using the following equation:

$$N_v = \frac{N_s - \overline{(N_{s,0} - N_{v,0,ref} \times M_0)}}{M} \qquad 6\text{-}1$$

where N_s is the fitted slant column density, N_v the vertical column, M the air mass factor, $N_{s,0}$ and M_0 are all fitted slant columns and corresponding air mass factors belonging to the reference sector.

6.2 DOAS spectral fitting

6.2.1 Reference radiance database

The DOAS fit, which will further explained in section 6.2.3, requires the measured radiances to be normalized by a reference irradiance spectrum. As mentioned before, it is also common, for the retrieval of tropospheric species to normalize them by another reference Earthshine spectrum taken in a remote region with expected low concentration levels of the species of interest in order to reduce systematic errors due to spectral interferences and/or instrumental limitations. For imager-types of instruments such as TROPOMI, one different reference mean radiance is used for every detector row in order to limit as much as possible stripes originating from imperfect cross-calibration and from different dead/hot pixel masks in different regions of the CCD.

In practice, the reference radiance spectra are generated for each row separately by averaging as many radiance spectra as possible geo-located within the equatorial Pacific sector (Latitudes: [-15° 15°], Long: [180°-240°]). This averaging procedure considers all observations recorded the same day as the orbit under treatment.

6.2.2 Wavelength recalibration

Generally speaking, the quality of a DOAS fit critically depends on the accuracy of the alignment between the earthshine radiance spectrum, the reference (solar irradiance) spectrum and the cross sections. Although the L1b data contain spectral assignment of the measurements, an accurate fine-tuned spectral calibration based on the Fraunhofer lines needs to be performed by the Level 1-2 DOAS algorithms. To this end, a reference solar atlas E_{ref} accurate in absolute vacuum wavelength to better than 0.001 nm (Chance and Kurucz, 2010) is degraded to the resolution of the instrument, through convolution by the instrumental slit functions.

Using a non-linear least-squares approach, the shift (Δ_i) between the reference solar atlas and the L1 irradiance is determined in a set of equally spaced sub-intervals covering a spectral range large enough to encompass all relevant fitting intervals. The shift is derived according to the following equation:

$$E_0(\lambda) = E_{ref}(\lambda - \Delta_i) \qquad 6\text{-}2$$

where E_{ref} is the reference solar spectrum convolved at the resolution of the instrument and Δi is the shift in sub-interval i. A polynomial (of order 3) is then fitted through the individual points $\Delta_i(\lambda_i)$, where λ_i is the centre wavelength of the sub-interval i, in order to reconstruct an accurate wavelength calibration $\Delta(\lambda)$ for the complete analysis interval. Note that this approach allows compensating for stretch and shifting errors in the original wavelength assignment.

In the case of imager-type of instruments, the procedure is complicated by the fact that such calibrations must be performed (and stored) for each separate spectral field on the CCD detector array. Indeed, due to the imperfect characteristics of the imaging optics, each detector row (ground pixel) of the TROPOMI instrument must be considered as a separate detector for analysis purposes.

In the actual DOAS fit, which follows this wavelength recalibration step, the absorption cross sections of the different trace gases must be used at the instrumental spectral resolution. The first option is to use the slit functions determined as part of the TROPOMI key data, which are available for the different measurement channels and for the different detector rows. Another approach is to characterize the slit functions as part of the wavelength calibration procedure in a dynamic way by fitting the main parameters of a predetermined line shape (e.g. asymmetric Gaussian) simultaneously to the shift Δ_i in each sub-interval i. The various cross-sections need then to be convolved dynamically using the slit function fitted during the wavelength calibration. This capability may be particularly useful if the real slit function turns out to differ significantly from the key data slit function or if the instrumental degradation leads to some slit function change over time. So far, this is not the case and we use the key data slit functions to preconvolve the cross-sections, which is much more efficient from a computational point of view.

More specifically, wavelength calibrations are made separately for every detector row of each S5p orbit by applying the different following steps:

0. Starting point: irradiance and radiance spectra given on their own wavelength grid (those assigned by the level 0-1 processor).
1. Regridding of the radiance: the radiance spectrum is interpolated on the irradiance (cubic spline), so that both spectra are given on the same wavelength grid.
2. Wavelength calibration: a procedure using an external reference solar atlas is applied to optimize the wavelength calibration of the solar irradiance. This procedure uses contiguous 7 sub-windows of approximately 10 nm width each ranging between 420 and 480 nm, which allows to compensate for shift and stretch effects as described above. This step is performed on the solar irradiance for 2 main reasons:
    a. The alignment with the solar reference atlas has best accuracy because solar lines are not distorted by atmospheric effects (e.g. due to molecular absorption or Ring effect)
    b. The calibration procedure (which can be relatively heavy if ISRF parameters are also fitted) has to be performed only once per orbit

2b. When using a mean radiance as the DOAS reference (rad-as-ref), this selected mean earthshine radiance is aligned on the solar irradiance by means of a DOAS fit, and the shift/stretch values determined in this procedure are used to recalculate the wavelength grid corresponding to the selected rad-as-ref. This wavelength grid becomes the reference grid for the rest of the analysis. Note that this approach is more accurate than applying the Kurucz calibration directly to the mean radiance, because the alignment (through the DOAS procedure) between two spectra acquired with the same instrument is extremely accurate, and (as already mentioned) the Kurucz procedure (making use of an external solar line reference) has best accuracy when applied to a solar irradiance.

3. Cross-section gridding: Absorption cross-sections are interpolated (cubic spline) on the optimized wavelength grid of the irradiance/rad-as-ref.
4. DOAS spectral fit (see next section): shift and stretch parameters (applied to the current radiance) are fitted to properly align all spectral items (irradiance or rad-as-ref, cross-sections and radiance).

6.2.3 DOAS spectral fitting

6.2.3.1 DOAS equations for nadir satellite measurements

Figure 3 sketches the geometry of a nadir satellite radiation measurement, defining the solar and viewing zenith angles (θ_0 and θ, with $\mu_0 = |cos\theta_0|$ and $\mu = |cos\theta|$) and the solar and viewing azimuth angles (φ_0 and φ) towards the zenith in a plane parallel atmosphere. Following the definitions adopted in [RD01], the angles are given at the surface (z = 0m).

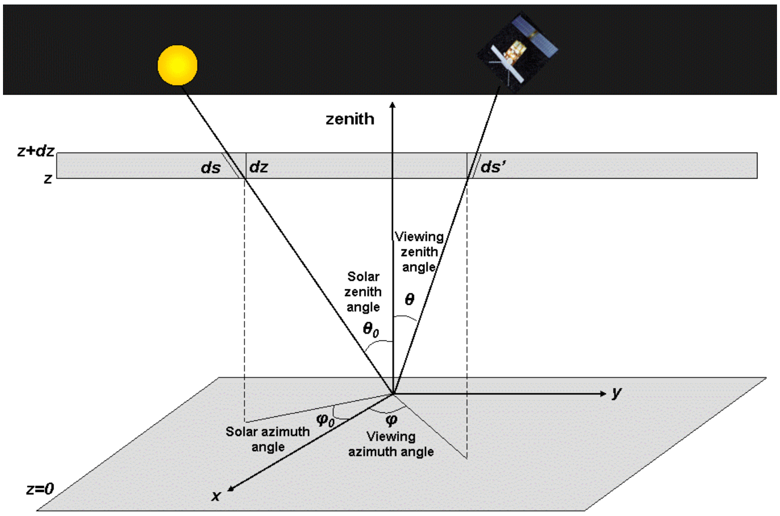

Figure 3: Sketch of satellite radiation measurement and geometry in a plane parallel atmosphere.

The DOAS method relies on the application of the Beer-Lambert law to the whole atmosphere. The backscattered earthshine spectrum as measured by the satellite spectrometer contains the strong solar Fraunhofer lines and additional fainter features due to interactions taking place in the Earth atmosphere during the incoming and outgoing paths of the radiation. The basic idea of the DOAS method is to separate broad and narrowband spectral structures of the absorption spectra in order to isolate the narrow trace gas absorption features. In practice, the DOAS approach relies on the following key approximations:

1. A single mean optical path is considered for photons traveling through the atmosphere towards the instrument. This allows expressing light attenuation in term of the Beer-Lambert's law and separating spectroscopic retrievals from radiative transfer calculations.
2. The absorption cross-sections are supposed to be weakly dependent on temperature and independent of pressure: this allows introducing the concept of one effective slant column density for the considered wavelength window.
3. Broadband variations are approximated by a common low-order polynomial to compensate for the effects of loss and gain from scattering and reflections by clouds and/or at the Earth surface.

1. A single "effective" light path is assumed which represents an average of the complex paths of all reflected and scattered solar photons reaching the instrument within the spectral interval used for the retrieval. This simplification is valid if the atmosphere can be considered as optically thin over the considered wavelength interval. The length of the effective light path is dealt with separately using radiative transfer calculations. By expanding Beer-Lambert's law, the various factors that influence the Earth reflectance at the top-of-atmosphere are considered by an equation that includes the effect of all absorbers present over the light path as well as Rayleigh and Mie scattering particles:

$$R(\lambda) = \frac{\pi I(\lambda)}{\mu_0 E_0(\lambda)} = \exp\left(-\int_0^{TOA}\left(\sum_j \sigma_j(\lambda,s)n_j(s) + \sigma_{Ray}(\lambda,s)n_{Ray}(s) + \sigma_{Mie}(\lambda,s)n_{Mie}(s)\right)ds\right)A(\lambda), \qquad \text{6-3}$$

where $I(\lambda)$ and $E_0(\lambda)$ are the measured earthshine backscattered radiance and solar irradiance spectra. μ_0 is the cosine of the solar zenith angle θ_0.

The integral is taken along the effective path followed by the photons through the atmosphere. The summation is performed over all relevant species with absorption cross-sections σ_j [cm^{2}molec.$^{-1}$] and densities n_j [molec.cm^{-3}]. σ_{Ray} and σ_{Mie} are the Rayleigh and Mie extinction cross-sections, while n_{Ray} and n_{Mie} are respectively the Rayleigh and Mie scattering particle densities. The densities of the absorbers and scattering particles vary with altitude along the light path. To a lesser extent, it is in principle also the case for the absorption cross-sections because of their dependence on temperature. Furthermore, the factor *A(λ)* describes the spectral broadband dependence of the measured radiance which is a complex function of the scattering efficiency of the Earth/atmosphere system and of the surface properties. It also effectively accounts for possible multiplicative errors in the measured reflectance, such as e.g. due to uncorrected instrument degradation effects, uncertainties in the radiometric calibration or possible residual (smooth) polarisation response effects not accounted for in the level 0-1 processing.

2. If it can be assumed that the absorption and scattering cross-sections σ do not depend on s, the sum over the individual terms and the integral can be exchanged, allowing the introduction of the slant column density ($N_{s,j} = \int_0^{TOA} n_j(s)ds$) in Equation 6-3:

$$\frac{\pi I(\lambda)}{\mu_0 E_0(\lambda)} = \exp\left(-\left(\sum_j \sigma_j(\lambda)\, N_{s,j} + \sigma_R(\lambda) N_{s,R} + \sigma_M(\lambda) N_{s,M}\right)\right) A(\lambda)\ , \tag{6-4}$$

This assumption is justified by the fact that the pressure dependence of absorption cross-sections can in most cases be neglected in the UV-Vis region. However, the temperature dependence of absorption cross-sections may be significant (for example that of NO_2). This can be corrected in first approximation by fitting two absorptions cross-sections at different temperatures assuming linear dependence on temperature (Van Roozendael et al., 2006). The latter approach is applied to the NO_2 absorption cross-sections during the fit of glyoxal.

3. Molecular absorption cross-sections $\sigma_j(\lambda)$ are usually highly structured, while scattering by molecules and particles, as well as reflection at the surface, have broadband spectral dependences that can be approximated by a low order polynomial. The final DOAS equation is obtained by considering the logarithm of (6-4) and including all broadband variations in a single polynomial:

$$\ln \frac{\pi I(\lambda)}{\mu_0 E_0(\lambda)} = -\sum_j \sigma_j^{diff}(\lambda)\, N_{s,j} + \sum_p c_p \lambda^p \tag{6-5}$$

$$\tau_s^{meas}(\lambda) = \tau_s^{diff}(\lambda, N_{s,j}) + \tau_s^{smooth}(\lambda, c_p), \tag{6-6}$$

where the measured optical depth τ_s^{meas} is separated into its highly structured part τ_s^{diff} and its broadband variation τ_s^{smooth}. Note that the absorption cross-sections σ_j are also separated into the so-called "differential absorption cross-sections" σ_j^{diff}, which represent the high-pass filtered parts of the absorption cross-sections, and the "low frequency absorption cross-sections" σ_j^{smooth}, that are taken over by the polynomial.

Equation (6-5) is a linear equation between the logarithm of the measured quantities (I and E_0), the slant column densities of all relevant absorbers ($N_{s,j}$) and the polynomial coefficients (c_p), at multiple wavelengths. DOAS retrievals consist in solving an over-determined set of linear equations, which can be done by standard methods of linear least squares fit (Platt and Stutz, 2008). The aim of the fitting process is to minimize the chi-square function, i.e. the weighted sum of squares derived from Equation (6-6):

$$\chi^2 = \sum_{i=1}^{k} \frac{\left(\tau_s^{meas}(\lambda_i) - \tau_s^{diff}(\lambda_i, N_{s,j}) - \tau_s^{smooth}(\lambda_i, c_p)\right)^2}{\varepsilon_i^2} \tag{6-7}$$

where the summation is made over the individual spectral pixels included in the selected wavelength range (k is the number of spectral pixels in the fitting interval). ε_i is the statistical uncertainty on the measurement at wavelength λ_i. Weighting the residuals by the instrumental errors ε_i is optional. When no measurement uncertainties are used (or no error estimates are available), all uncertainties in Equation (6-7) are set to $\varepsilon_i = 1$, giving all measurement points equal weight in the fit.

Another measure for the goodness of the fit is the so-called root-mean-squared (RMS) error, which is defined as follows:

$$\mathrm{RMS} = \sqrt{\frac{\sum_{i=1}^{M}\left(\tau_s^{meas}(\lambda_i) - \tau_s^{diff}(\lambda_i, N_{s,j}) - \tau_s^{smooth}(\lambda_i, c_p)\right)^2}{k}} \qquad \text{6-8}$$

In order to optimize the fitting procedure, additional structured spectral effects have to be considered carefully such as the Ring effect (Grainger and Ring, 1962). Furthermore, the linearity of Equation (6-5) may be broken down by instrumental aspects such as small wavelength shifts between I and E_0, which requires accurate calibration.

In practice, instead of normalizing the Earthshine backscattered radiance by the solar irradiance $E_0(\lambda)$, it is common for the retrieval of tropospheric species to normalize the individual radiances by the mean of a set of radiances falling in a reference sector where low concentrations of the gas of interest are expected (see section 6.2.1). Any bias in the fitted slant column introduced by a possible residual absorption signature in the mean reference spectrum is removed by the normalization procedure described in section 6.4.

6.2.3.2 Glyoxal slant column retrieval

Glyoxal has significant absorption bands in the visible part of the spectrum (Figure 4). However, its low atmospheric concentrations (maximum 5-10x10^{14} molec.cm^{-2}) make the glyoxal optical depth very small (~5e^{-4}) compared to other species absorbing in the same spectral region. For example, the NO_2 optical depth in a polluted region will be typically 20 times than that of glyoxal. This makes the retrieval of glyoxal very challenging, as spectral interferences with other species may have large impact on the retrieved glyoxal columns. Also because of this low optical depth, glyoxal products generated from space nadir observations have a high level of noise, making averages in time and/or space necessary to produce physically meaningful glyoxal fields. The choice of an optimal fitting window may be of crucial importance to reduce as much as possible both the noise and spectral interferences with other absorbers in the retrieval. For glyoxal, the small number of absorption bands limits the number of possible fit intervals. Important spectral structures related to Ring effect (inelastic scattering) prevents the exploitation of the first glyoxal absorption band below 430 nm (Vrekoussis et al., 2009). The first glyoxal retrievals from space have exploited the SCIAMACHY measurements between 436 and 457 nm (Wittrock et al., 2006). Lerot et al. (2010) have found empirically that the fit window 435-460 nm was well adapted to retrieve glyoxal from GOME-2/Metop-A observations. This interval appears also to be well suited for the OMI instrument. More recently, two different studies (Alvarado et al., 2014; Chan Miller et al., 2014) have been conducted to determine optimal glyoxal retrievals in a more systematic way using OSSE experiments. The two studies have shown that optimal intervals encompass the two larger absorption bands. They have also shown that results based on OSSEs may also significantly differ from experiments based on real data, owing to the possible limitations of the forward models used in those OSSEs. Alvarado et al. (2014) found an optimal interval ranging from 433 and 458 nm, while Chan Miller et al. (2014) have used the interval 435-461 nm, the two being very close the fitting window proposed in this S5p scientific algorithm (435-460 nm).

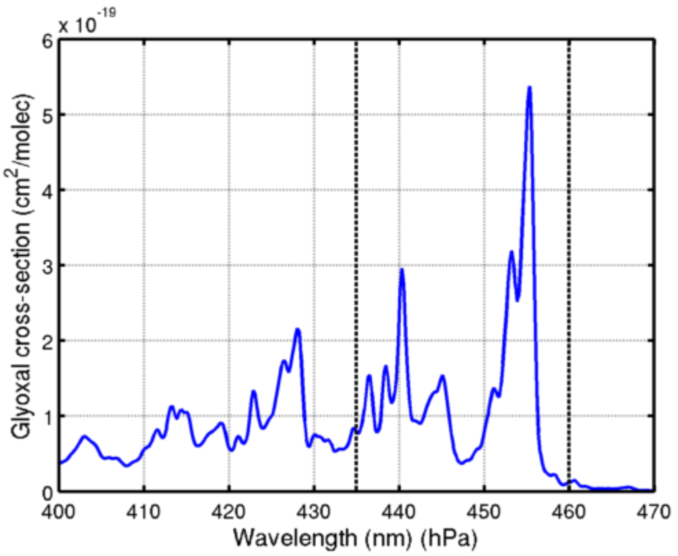

Figure 4: Glyoxal absorption cross-section in the visible convolved at the GOME-2/Metop-A spectral resolution. The dashed lines indicate the fitting window of the baseline retrieval algorithm 435-460 nm.

6.2.3.3 Fitting intervals, absorption cross-sections and retrieval settings

As mentioned before, over remote oceanic regions, a spectral signature from clean liquid water (Figure 5) significantly interferes with the fit of glyoxal, leading to a strong negative bias in the retrieved columns if not properly accounted for (Lerot et al., 2010). For the GOME-2/Metop-A instrument, a correction was proposed that relied on a two-step DOAS retrieval approach, i.e. a 1st fit in a wide interval to derive the liquid water optical depth, which is then prescribed in the a 2nd fit to retrieve the glyoxal slant column.

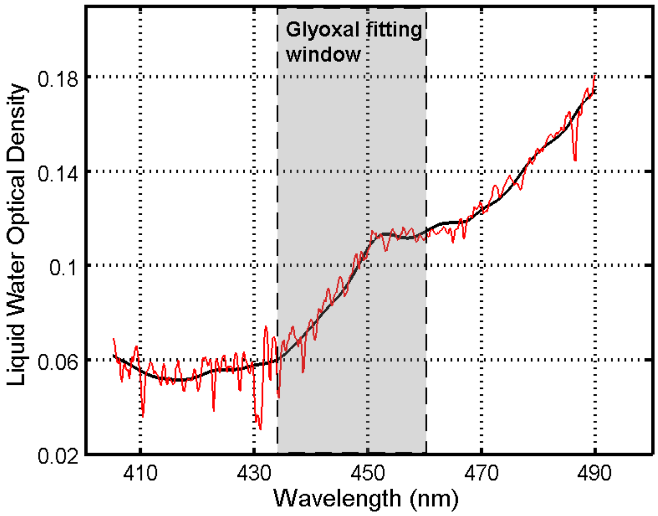

Figure 5: Illustration of the typical liquid water optical depth in the visible region over remote oceans. If not properly taken into account, this signature cross-correlates with glyoxal, leading to significant biases.

However, more recent studies based on OMI observations (e.g. Alvarado et al. (2014)) have shown that fitting simultaneously the liquid water and glyoxal in a single small interval performs as good as the two-step approach. Also, this easier approach has been tested on TROPOMI spectra and this led to similar conclusions. Therefore, the glyoxal slant columns are retrieved using one single DOAS fit in the interval 435-

460nm. In addition to glyoxal, absorption cross-sections are also included for the liquid water, ozone, O_4, water vapour, NO_2 (at two temperatures), and for the Ring signature. The Ring spectrum is calculated as in (Chance and Spurr, 1997) using the recent reference solar atlas (Chance and Kurucz, 2010).

Two additional cross-sections are used within to DOAS fit to account for along-track scene heterogeneity. Indeed, similarly to OMI, the S5p spectrometer slit is perpendicular to flight direction with the consequence that any intensity variation along track leads to spectral shifts and perturbations of the instrumental response slit function (Noël et al., 2012; Voors et al., 2006). As it has been shown for NO_2 (Richter, 2018), those perturbations have a direct impact on the quality of the DOAS fits (increase of the fit residuals) and may also lead to systematics biases on the retrieved glyoxal slant columns. Such abrupt intensity changes occur for example along the cloud edges but also along coasts. For example, Figure 6 shows in the panel (a) that the root mean square (RMS) of the DOAS fit residuals is systematically higher along the coasts but also over land where contamination by broken clouds or abrupt elevation changes cause discontinuities in brightness fields. The stripes visible in this figure are due to the smaller pixel size (and hence lower signal-to-noise ratio) on the edges of the across-track field of view. The panel (c) shows that there are some collocated artificial patterns (positive/negative biases) in the mean retrieved glyoxal slant column field. The latter result from spectral interferences with the signature introduced by the ISRF distortion. Following the approach described in (Richter, 2018), pseudo cross-sections reproducing the spectral signature due to this ISRF perturbation can be introduced in the DOAS fit and hence minimize spectral interferences with other species, including glyoxal. With those additional cross-sections, the fit quality of heterogeneous scenes improves and systematic biases on the retrieved slant columns are reduced as shown in panels (b) and (d) of Figure 6 where both the glyoxal along the coasts and the pseudo-noise are reduced. The cross-sections are generated with a statistical analysis of the fit residuals for many observations in the Pacific Ocean as a function of the level of scene heterogeneity. The latter can be computed using radiance measurements at higher spatial resolution available in the TROPOMI level-1 data at a limited number of wavelengths. It ranges between -1 and +1 and is close to/deviates from 0 for homogenous/heterogeneous scenes, the sign indicating the part of the ground pixel that dominates the scene brightness. The cross-sections correspond to the systematic residuals of scenes with a heterogeneity factor larger/smaller than +/- 0.08. Note that a third cross-section derived from the mean residuals of homogeneous scenes is also added, which explains why the fit RMS are also reduced (but less drastically) in homogeneous scenes. This cross-section has no impact on the retrieved glyoxal SCDs and allowed mostly isolating systematic residuals due to scene heterogeneity only for the pseudo cross-sections creation.

As aforementioned (section 6.2.1), instead of using the daily solar irradiance to compute the reflectance (6-4), we use daily averaged radiances, selected for each detector row, in the reference equatorial Pacific sector. This approach allows to significantly reduce the row-dependent instrumental artefacts and to limit the impact of the possible degradation of the detectors. This is nevertheless complemented by an additional background/destriping correction procedure (section 6.4). The DOAS settings used to retrieve CHOCHO SCDs are summarized in Table 2.

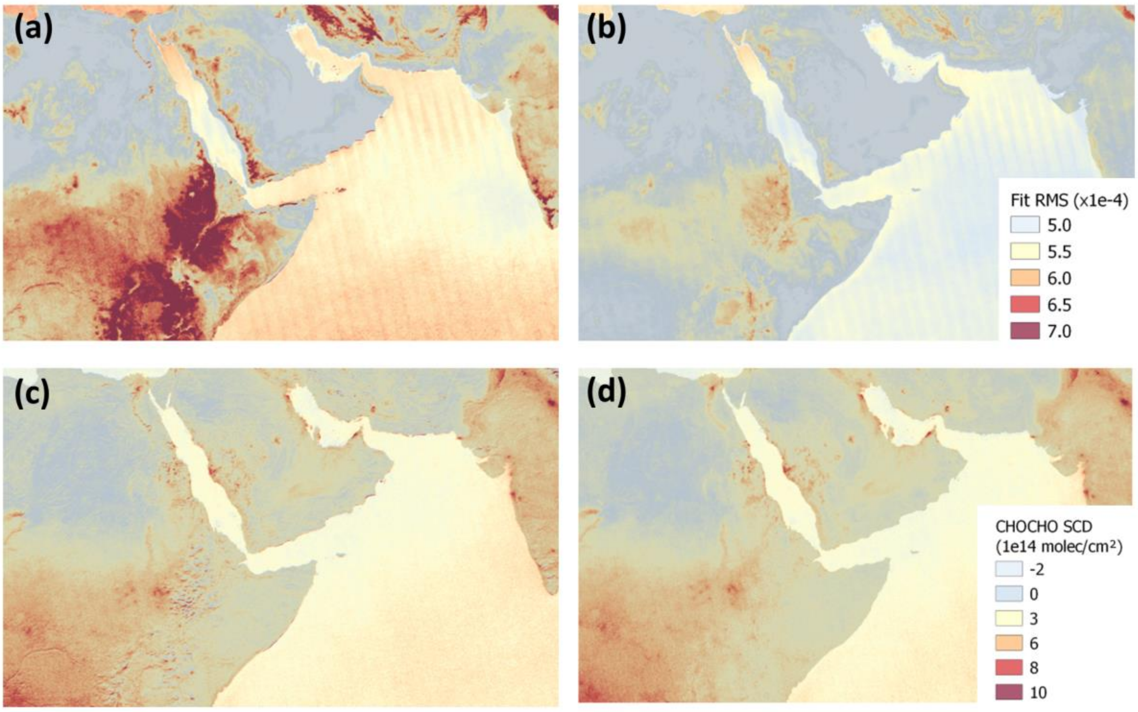

Figure 6: Impact of scene brightness heterogeneity on glyoxal retrievals in the fitting window 435-460 nm over the Horn of Africa and Middle-East. The panels (a) and (b) show mean fit residuals RMS for the year 2019 without and with (left and right) pseudo-cross sections to correct for spectral signatures introduced by scene heterogeneity. The panels (c) and (d) show the corresponding mean glyoxal slant column densities. Only observations with cloud fractions less than 20% are considered.

Table 2: Summary of DOAS settings used to retrieve glyoxal slant columns from TROPOMI spectra.

Fitting interval	**435-460 nm**
Absorption cross-sections	
Glyoxal	Volkamer et al. (2005)
Ozone	Serdyuchenko et al. (2014), 223K
H_2O (vapor)	Rothman et al. (2013), 293K
NO_2	Vandaele et al. (1998), 220 and 294K
O_4 (O_2-O_2)	Thalman and Volkamer (2013), 293K
H_2O (liquid)	Mason et al. (2016)
Scene Heterogeneity	2 pseudo-absorbers (Richter, 2018) + common residuals – Internally generated
Ring effect	Pseudo-absorber (Chance and Spurr, 1997)
Slit function	**Baseline**: 1 slit function per binned spectrum as a function of wavelength (Pre Flight Model) Option: fit of a prescribed function shape to determine the ISRF during wavelength calibration + online convolution of cross-sections (not needed so far).
Polynomial	3rd order
Intensity offset correction	1st-order offset (additional cross-section taken as the invert of the reference spectrum)
Earthshine wavelength Doppler-shift	1st-order shift
Reference spectrum (E_0)	Daily average of radiances, per detector row, selected in equatorial Pacific ([-15° 15°], Long: [180°-240°])

6.2.3.4 Spike removal algorithm

A method to remove individual hot pixels or pixels affected by the South Atlantic Anomaly has been presented for NO_2 retrievals in Richter et al. (2011). Often only a few individual detector pixels are affected and in these cases, it is possible to identify and remove the noisy points from the fit. However, as the amplitude of the distortion is usually only of the order of a few percent or less, it cannot always be found in the highly structured spectra themselves. Higher sensitivity for spikes can be achieved by analysing the residual of the fit where the contribution of the Fraunhofer lines, scattering, and absorption is already removed.

When the residual for a single pixel exceeds the average residual of all pixels by a chosen threshold ratio (the tolerance factor), the pixel is excluded from the analysis and the DOAS fit is repeated in an iterative process. This procedure is repeated until no further outliers are identified, or until the maximum number of iterations is reached (here fixed to 3). Tests performed with GOME-2 and OMI spectra show that a tolerance factor of 5 improves the glyoxal fits. This is especially important to handle the degradation of 2-D detector arrays such as OMI or TROPOMI.

6.2.3.5 Empirical correction for strong NO_2 absorption

The DOAS approach assumes that the wavelength dependence of the effective light path within the fit interval can be neglected. Although this assumption is generally reasonable, it may fail in case of strong absorption by one (or more) species, of which the slant column density becomes dependent on the wavelength (Puķīte et al., 2010). In that case, fitting the optical depth of that species by a simple scaling of its cross-section is inaccurate and the fit quality is degraded. Puķīte et al. (2010) have shown that fitting additional cross-sections resulting from a Taylor expansion of the wavelength-dependent slant column corrects for its variability within the fit window. As mentioned before, the high sensitivity of glyoxal retrievals to potential sources of misfit was a motivation to further investigate its sensitivity to extreme NO_2 concentration levels.

For this purpose, synthetic spectra were generated at a spectral resolution of 0.5 nm with the radiative transfer model SCIATRAN (Rozanov et al., 2005) for a satellite nadir-viewing geometry and two different solar zenith angles. In those simulations, inelastic scattering was neglected and a large range of tropospheric NO_2 columns was covered by scaling the NO_2 a priori profile. The TROPOMI DOAS baseline described above was then applied to those simulated spectra in order to retrieve CHOCHO SCDs and evaluate the error as a function of the NO_2 SCD as illustrated in Figure 7. Results clearly point to a CHOCHO SCD error increasing with the NO_2 SCD. Note that the exact error magnitude may change slightly depending on the NO_2 vertical distribution and on the actual atmospheric content. On the other hand, adding two so-called Pukite cross-sections (Puķīte et al., 2010) resulting from a first order expansion of the NO_2 slant column around the wavelength and the vertical optical depth significantly reduces the errors.

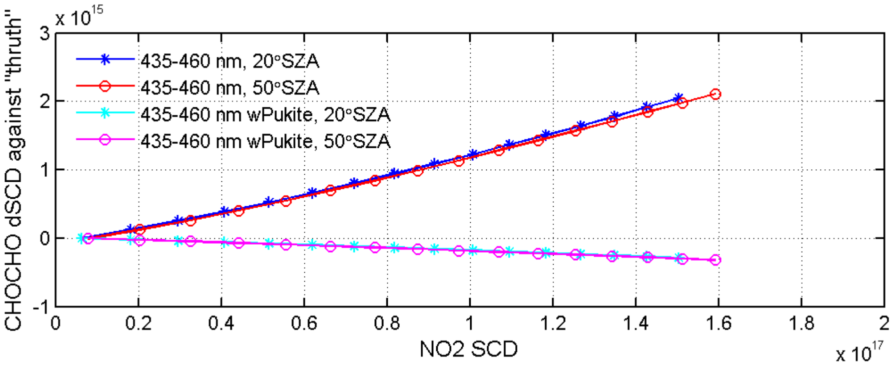

Figure 7: Absolute error (in molec/cm²) on the retrieved CHOCHO SCD as a function of the NO_2 SCD for simulated spectra in a nadir-viewing satellite geometry and for two solar zenith angles. The reference "true" CHOCHO SCD is taken as the value retrieved for the lowest NO2 SCD scenario. The error increases with the NO_2 SCD when Pukite cross-sections are not included in the fit, but remains small otherwise.

On this basis, the impact of adding the Pukite cross-sections to the DOAS baseline has been investigated using one month of TROPOMI data. A wintertime period was chosen (December 2019) to favour the number of observations with large NO_2 concentrations, in particular in China but also in other megacities in the Northern Hemisphere. Figure 8 (upper panel) displays the monthly mean NO_2 SCDs in December 2019, and (middle panel) the mean impact on the retrieved CHOCHO SCDs of introducing the Pukite terms in the DOAS spectral fit baseline. The CHOCHO SCD differences caused by the Pukite terms are also plotted as a function of the NO_2 SCDs to better visualize the correlation (lower panel). For regions with enhanced NO_2 concentrations (>$2x10^{16}$ molec/cm²) (e.g. China, India, Teheran), the Pukite cross-sections lead to a systematic reduction of the CHOCHO SCDs, consistent with the closed-loop tests described above. A small improvement of the fit quality is found (not shown). Unexpectedly, the impact of those additional cross-sections on the CHOCHO SCDs can also be non-negligible in regions with low NO_2 columns: positive differences are for example observed over equatorial oceans, but also over South America and Africa. The correlation plot of Figure 8 clearly shows these two regimes. While the impact of the Pukite cross-sections on the glyoxal retrievals is understood and reliable for large NO_2 SCDs, their influence at low NO_2 SCD is more questionable and likely results from spectral interferences occurring between the different fitted spectra (e.g. with the Ring signature), which introduces additional noise in the product. To avoid this, rather than fitting additional cross-sections, we introduce an empirical correction applied to the glyoxal SCDs. This correction consists in subtracting from the glyoxal SCD a NO_2-SCD dependent value, directly prescribed from the linear regression fit through the sensitivity test results for all observations worldwide from December 2019, with NO_2 SCDs larger than $2x10^{16}$ molec/cm² as illustrated in Figure 8 (c). It is worth noting that the regression fit results agree well with the glyoxal SCD errors estimated from the simulations presented above (Figure 7). For extreme pollution conditions such as what can be found in China during Wintertime, this correction may lead to glyoxal column reduction up to 30%.

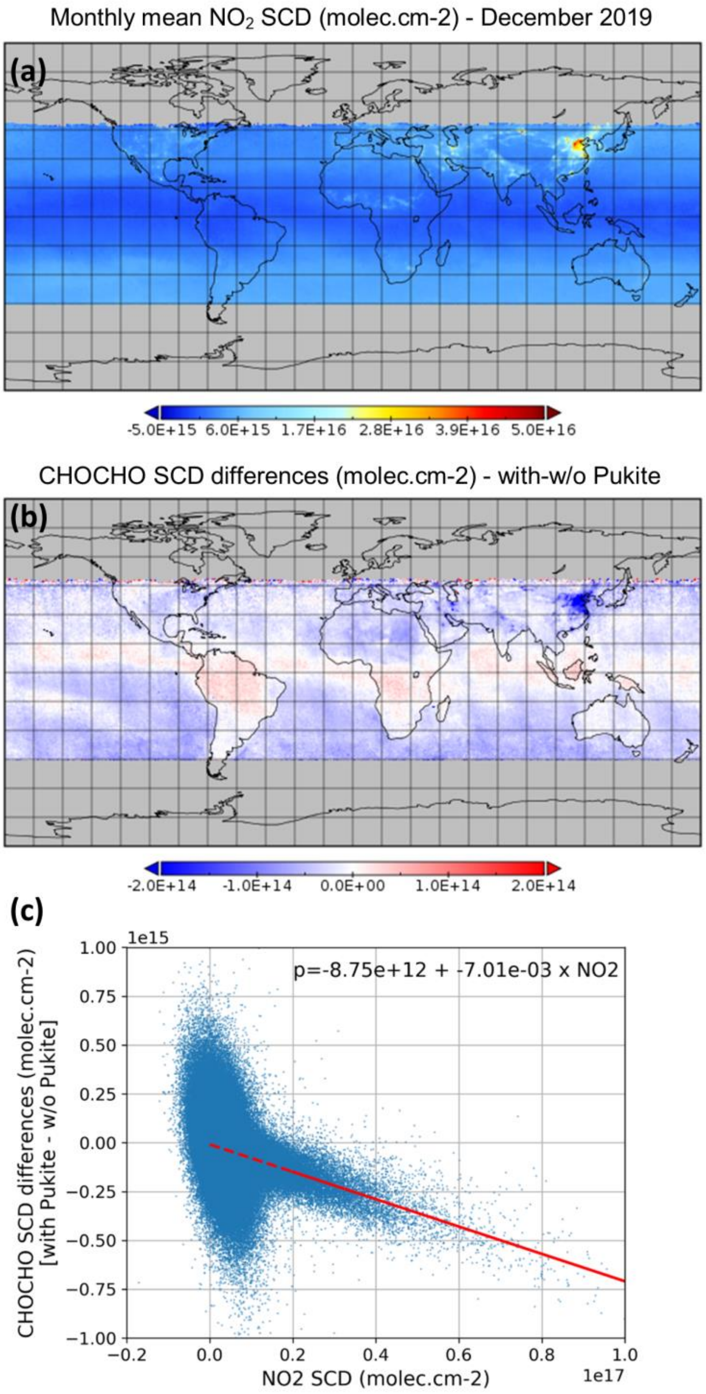

Figure 8: (a) Monthly mean NO$_2$ SCDs retrieved from TROPOMI data in December 2019. Panel (b) illustrates the CHOCHO SCD absolute differences (molec/cm^2) due to the incorporation of the Pukite et al. (2010) cross-sections in the DOAS spectral fit and panel (c) shows the correlation between those differences and the NO$_2$ SCDs. The red line corresponds to a linear regression fit through all points with NO$_2$ SCD larger than 2x10^{16} molec/cm^2.

6.3 Tropospheric air mass factor calculation

In the DOAS approach, an optically thin atmosphere is assumed. The mean optical path of scattered photons can therefore be considered as independent of the wavelength within the relatively small spectral interval selected for the fit and a single wavelength effective air mass factor can be defined as the ratio of the slant column to the vertical column of a particular absorber j:

$$M_j = \frac{N_{s,j}}{N_{v,j}} \ . \tag{6-9}$$

In the troposphere, scattering by air molecules, clouds and aerosols leads to complex altitude-dependent air mass factors. Full multiple scattering calculations are required for the determination of the air mass factors, and the vertical distribution of the absorber has to be assumed *a priori*. For optically thin absorbers, the formulation of (Palmer et al., 2001) is conveniently used. It decouples the measurement vertical sensitivity to atmospheric species from the vertical profile shape of the species of interest:

$$M = \frac{\sum_l m_l(\lambda,\theta_0,\theta,\varphi,A_s,p_s)\, n_{al}(lat,long,time)}{\sum_l n_{al}(lat,long,time)}, \tag{6-10}$$

where m_l and n_{al} are respectively the altitude dependent air mass factor (see section 6.3.1) and the a priori vertical profile (see section 6.3.2) in each defined vertical layer *l*. A_s is the surface albedo, p_s is the surface pressure.

The altitude-dependent air mass factors represent the sensitivity of the slant column to a change in the partial columns $N_{v,l}$ in a certain atmospheric layer. In a scattering atmosphere, m_l depends on the wavelength, the sun and viewing angles, the surface albedo, and the surface pressure, but not on the vertical distribution of the considered absorber (optically thin approximation).

6.3.1 LUT of altitude dependent air mass factors

Generally speaking, m depends on the wavelength, as scattering and absorption processes vary with wavelength. However, the amplitude of the m variation is found to be small (generally less than 5%) in the 435-460 nm fitting window and a single air mass factor representative for the entire wavelength interval is used (at 448 nm).

Figure 9 illustrates the dependency of m with the solar and viewing angles, θ_0, θ, and with scene albedo and altitude. The decrease of sensitivity in the boundary layer is clearly visible for low albedo scenes as the contribution of scattered light is larger than the light reflected by the ground. For larger surface albedo, the reflected light contributes more significantly increasing the sensitivity to the boundary layer glyoxal concentrations. The relative azimuth angle does have relatively less impact on the measurement sensitivity.

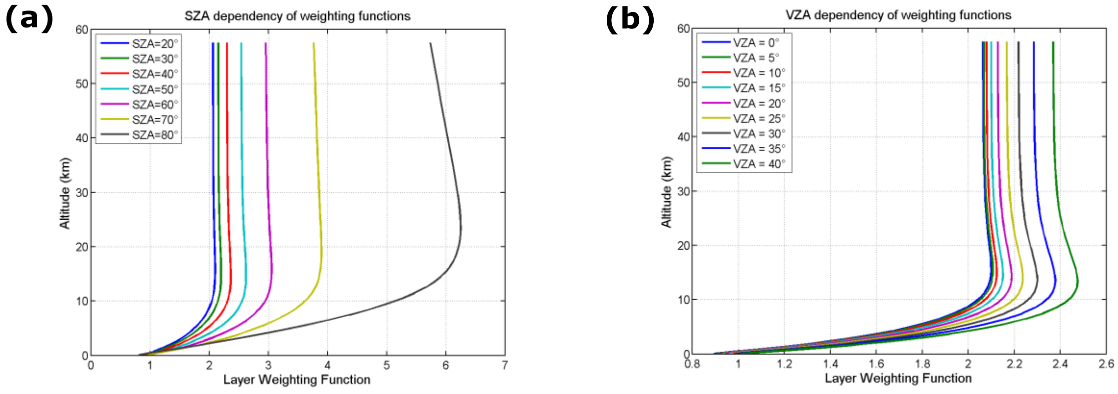

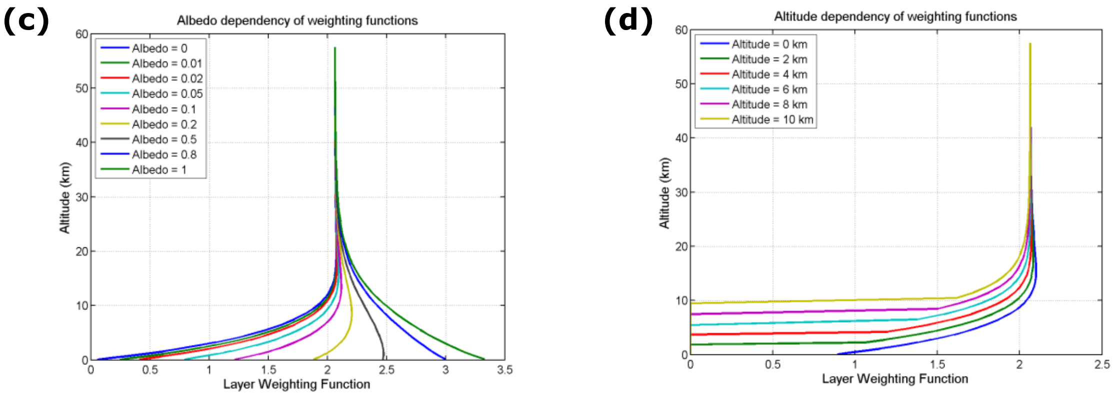

Figure 9: Variation of the altitude dependent air mass factor (or layer weighting functions) at 448 nm with: (a) solar zenith angle, (b) viewing zenith angle, (c) surface albedo, (d) surface altitude. Unless specified, the parameters chosen for the radiative transfer simulations are: SZA=30°, VZA=0°, RAA=0°, albedo=0.05, surface pressure=1013hPa.

Altitude-dependent air mass factors are calculated with the VLIDORT v2.7 radiative transfer model (in vector mode) (Spurr and Christi, 2019, [URL02]), at 448 nm, using a US standard atmosphere, for a number of representative observation geometries, surface albedos and surface pressures, and stored in a look-up table. Altitude-dependent air mass factors are then interpolated within the lookup table for each particular observation conditions and interpolated vertically on the pressure grid of the a priori profile. Linear interpolations are performed in $\cos(\theta_0)$, $\cos(\theta)$, relative azimuth angle (the latter being computed using SAA and VAA provided in the L1b radiance product) and surface albedo, while a nearest neighbour interpolation is performed in surface pressure. The parameter values chosen for the look-up table are detailed in Table 3. With such a granularity, the LUT size is about 40 MB. In particular, the grid of surface pressure is very thin near the ground, in order to minimise interpolation errors caused by the generally low albedo of ground surfaces. Indeed, as illustrated by Figure 9 (panel d), the altitude-dependent air mass factors vary in a discontinuous way with surface elevation, especially for dark surfaces. Furthermore, the LUT and model pressures are scaled to the respective surface pressures, in order to avoid extrapolations outside the LUT range.

Every TROPOMI observation requires thus an interpolation through the altitude-dependent AMF LUT. While the observation angles are extracted from the L1b data along with the spectral data, the scene altitude and reflectivity have to be provided by external input data. The sensitivity to the lowermost layers of the atmosphere and to the surface is higher in the visible spectral range than in the ultraviolet. The a priori knowledge of the surface albedo is therefore very important, and potentially an important source of error. Ideally, LER databases covering the visible spectral range and constructed at the S5p overpass time with a spatial resolution close to the TROPOMI ground pixel size should be used. Also, it would be valuable to account somehow for the anisotropy in the surface reflection either by the use of a BRDF product if available or at least by the use of a directionally-dependent LER climatology as the neglect of this effect may introduce significant errors (Lorente et al., 2018). Such an ideal database is currently not available and the current baseline is to use the OMI LER climatology (Kleipool et al., 2008), which has a spatial and time resolution of 0.5° x 0.5° and one month, respectively. This climatology provides both mode values and minimum values. The latter are used to avoid as much as possible the presence of residual contamination by snow/ice/clouds. For every TROPOMI observation, the appropriate albedo value is extracted from the database by simple linear interpolations. Although the overpass time of OMI is similar to that of S5P, the resolution of that climatology is too coarse and neglects the observation geometry dependence. There are some on-going efforts to exploit the TROPOMI data in order to construct more suited data sets, which will contribute to reduce the uncertainties related to the knowledge of the surface reflectivity (e.g. (Loyola et al., 2019)). Such future databases will be tested later in the project. The sensitivity of the nadir-viewing instruments to the lowermost layer of the atmosphere also depends on the ground elevation. This aspect is easier to address than the ground reflectivity as its variability in time is generally negligible and such an information is available at much higher resolution than our needs. We use the GMTED2010 data set that has a spatial resolution up to 7.5-arc-second (Danielson and Gesch, 2011). This database is degraded at a coarser resolution (~10km), more representative of the TROPOMI measurements as described in [RD08]. Note that we actually extract dynamically the surface altitude for every observation from the operational NO2 product

[RD09]. The latter uses the same database degraded at a coarser resolution. This avoids repeating similar operations and the NO_2 product is needed for other input data (see below).

Table 3: Parameters in the altitude-dependent air mass factors lookup table

Parameter name	Nb. of grid points	Grid of values	Symbol
Solar zenith angle [deg]	17	0, 10, 20, 30, 40, 45, 50, 55, 60, 65, 70, 72, 74, 76, 78, 80, 85	θ_0
Viewing zenith angle [deg]	10	0, 10, 20, 30, 40, 50, 60, 65, 70, 75	θ
Relative azimuth angle [deg]	5	0, 45, 90, 135, 180	φ
Surface albedo	14	0, 0.01, 0.025, 0.05, 0.075, 0.1, 0.15, 0.2, 0.25, 0.3 0.4, 0.6, 0.8, 1.0	A_s
Surface pressure [hPa]	17	1063.10, 1037.90, 1013.30, 989.28, 965.83, 920.58, 876.98, 834.99, 795.01, 701.21, 616.60, 540.48, 411.05, 308.00, 226.99, 165.79, 121.11	p_s
Atmospheric pressure [hPa]	64	1056.77, 1044.17,1031.72, 1019.41, 1007.26, 995.25, 983.38, 971.66, 960.07, 948.62, 937.31, 926.14, 915.09, 904.18, 887.87, 866.35, 845.39, 824.87, 804.88, 785.15, 765.68, 746.70, 728.18, 710.12, 692.31, 674.73, 657.60, 640.90, 624.63, 608.58, 592.75, 577.34, 562.32, 547.70, 522.83, 488.67, 456.36, 425.80, 396.93, 369.66, 343.94, 319.68, 296.84, 275.34, 245.99, 210.49, 179.89, 153.74, 131.40, 104.80, 76.59, 55.98, 40.98, 30.08, 18.73, 8.86, 4.31, 2.18, 1.14, 0.51, 0.14, 0.03, 0.01, 0.001	p_l
Altitude corresponding to the atmospheric pressure, using an US standard atmosphere [km] (for information)	64	-0.35, -0.25, -0.15, -0.05, 0.05, 0.15, 0.25, 0.35, 0.45, 0.55, 0.65, 0.75, 0.85, 0.95, 1.10, 1.30, 1.50, 1.70, 1.90, 2.10, 2.30, 2.50, 2.70, 2.90, 3.10, 3.30, 3.50, 3.70, 3.90, 4.10, 4.30, 4.50, 4.70, 4.90, 5.25, 5.75, 6.25, 6.75, 7.25, 7.75, 8.25, 8.75, 9.25, 9.75, 10.50, 11.50, 12.50, 13.50, 14.50, 16.00, 18.00, 20.00, 22.00, 24.00, 27.50, 32.50, 37.50, 42.50, 47.50, 55.00, 65.00, 75.00, 85.00, 95.00	z_l

6.3.2 A priori vertical profile shapes

Glyoxal concentrations peak near the surface because of the short lifetime of its NMVOC precursors emitted mostly at the ground. The profile shape varies according to local atmospheric NMHC sources, boundary layer depth, photochemical activity, and other factors. A priori glyoxal profiles can be provided by a limited number of global Chemical Transport model. Currently the glyoxal breadboard algorithm relies on a priori glyoxal profiles simulated by the CTM MAGRITTE developed at BIRA-IASB, which inherits from the IMAGES model (Bauwens et al., 2016; Müller and Brasseur, 1995; Stavrakou et al., 2009, 2013). The MAGRITTE model, run globally at 1°x1° resolution, calculates the distribution of 175 chemical compounds, of which 136 species undergo transport. In the vertical, the modelled troposphere is divided in 40 levels between the Earth's surface and the lower stratosphere. The meteorological fields are provided by ECMWF ERA-Interim analyses. The chemical mechanism and deposition scheme have been recently updated (Müller et al., 2018, 2019). It has to be noted that those CTM simulations are performed based on consolidated input data (emission inventories) when available. For this activity, the related delay is not problematic, but this approach would not be feasible in an operational processing context, which would require forecast capability from the CTM. At the moment, neither the CTM TM5 used for the TROPOMI operational processing, nor CAMS, which will be used for the Sentinel-4 and -5 processors, are able to model glyoxal fields. This issue has been addressed in [RD10].

Also, non-negligible glyoxal columns have been detected over some oceanic regions of the world (Coburn et al., 2014; Lerot et al., 2010; Sinreich et al., 2010). The sources for those elevated glyoxal concentrations are not well understood and therefore oceanic profiles calculated by current CTMs are not reliable. During the TORERO ("Tropical Ocean tRoposphere Exchange of Reactive halogens and Oxygenated hydrocarbons") campaign realized in January-February 2012, glyoxal concentration profiles have been measured with an Air-borne MAX-DOAS instrument over Pacific (Volkamer et al., 2015). Therefore, we use one of those measured profiles as a priori for the AMF computations for all satellite pixels over oceans instead of using the uncertain output of a CTM. The land classification flag provided in the operational NO_2 product is used to discriminate pixels over lands and oceans.

To reduce the errors associated to the topography and the lower spatial resolution of the model compared to the TROPOMI spatial resolution, the a priori profiles need to be rescaled to the effective surface elevation of the satellite pixel. Following Zhou et al. (2009), the surface pressure $p_{s,MAG}$ provided by the CTM MAGRITTE is converted by applying the hypsometric equation and the assumption that temperature changes linearly with height:

$$p'_s = p_{s,MAG}\left(\frac{T_s}{(T_s + \Gamma(z_{s,MAG} - z_s))}\right)^{-\frac{g}{R\Gamma}} \qquad 6\text{-}11$$

where T_s is the surface temperature (set to 273K), $\Gamma = 6.5K\ km^{-1}$ is the lapse rate, $R=287\ J\ kg^{-1}\ K^{-1}$ is the gas constant for dry air, and $g = 9.8\ ms^{-2}$ the gravitational acceleration. While z_s is the surface elevation for the satellite ground pixel (as previously used for the BAMF interpolation), $z_{s,MAG}$ is the terrain height representative for the model spatial resolution and is approximated by degrading the GMTED2010 database at 1°x1°. The pressure levels for the a priori CHOCHO profiles need to be redefined considering this improved surface pressure. For this, the climatological pressure grid p is rescaled by the factor $p'_s/p_{s,MAG}$.

6.3.3 Cloud and aerosols

As mentioned before, the low atmospheric glyoxal optical depths make its retrieval particularly sensitive to spectral interferences with other species absorbing in the same region (e.g. Ring, O_4…). As a consequence of those interferences, glyoxal slant columns tend to increase artificially over bright scenes such as snow covered surfaces or cloud-contaminated pixels. Because of this, it is recommended to apply a stringent filtering to eliminate all cloudy pixels. To do that, all pixels with an effective cloud fraction f_c retrieved simultaneously to the NO_2 columns in the visible spectral range [RD09] should have a low qa_value (see section 6.5.5) in order to be discarded by the user. The impact of residual clouds in remaining pixels is simply neglected. The approach is therefore a bit simpler than in other products where the cloud filtering is less strict, but a cloud correction based on the independent approximation is applied (Boersma et al., 2004; Martin, 2002). For the reason mentioned before, the snow-covered scene should also have low qa_values to be discarded as well by users. The snow/ice flag provided by the National Snow and Ice Data Center NSIDC will be used as input of the qa_value computation (section 6.5.5)

The presence of aerosol in the observed scene may also affect the quality of the retrieval. No explicit treatment of aerosols (absorbing or not) is foreseen in the baseline algorithm as there is no general and easy way to treat the aerosols effect on the retrieval. The absorbing aerosol index (AAI) is provided in the L2 files and any pixel with high AAI should be used and interpreted with care.

6.4 Across-track background/destriping correction

Residual systematic biases in the retrieved columns, due to unresolved spectral interferences, are known to remain a limiting factor for the retrieval of weak absorbers such as glyoxal. Furthermore, in the case of a 2D-detector array such as TROPOMI, across-track striping can possibly arise, due to imperfect cross-calibration and different dead/hot pixel masks for the CCD detector regions. This instrumental effect can also be found for scanning spectrometers, but since these instruments only have one single detector, such errors do not appear as stripes, but rather as constant, unknown offsets. Across-track corrections are also meant to handle the time-dependent degradation of the instrument, as it was needed in the case of OMI and the so-called stripe artefact (Boersma et al., 2011).

These different retrieval artefacts can be compensated (up to a certain extent) using normalization approaches, such as the reference sector correction, that has been applied in retrievals of various species (e.g Alvarado et al., 2014; Lerot et al., 2010; De Smedt et al., 2015). The general idea is to add (row-dependent) correction values to the retrieved slant columns to ensure that their mean values in a reference sector agree with known reference slant columns $N_{s,0,ref} = N_{v,0,ref} \times M_0$. The reference sector is generally chosen in the central Pacific Ocean, where CHOCHO concentrations are expected to be low. Because of the limited knowledge on possible mechanisms producing glyoxal in those remote oceanic regions, the reference value $N_{v,0,ref}$ taken as being 1x10^{14} molec.cm^{-2} is somewhat arbitrary. This value might change in case of progress for modelling CHOCHO fields over oceanic regions.

In practice, the normalization procedure is applied on a daily basis in different steps to correct for different sources of biases:

1. The first step (row-dependent correction) consists in destriping the product. It relies on row-averaged slant columns $N_{s,0}$ computed using only pixels with latitudes in the range [15°S-15°N] and longitudes comprised between 165°E and 220°E. We substract from all SCDs N_s those mean row-dependent values before adding the reference slant column $N_{s,0,ref}$ computed for each row *r*. After this step, we have

   $$N'_s(r) = N_s(r) - N_{s,0}(r) + N_{v,0,ref} \times \overline{M_0(r)}, \qquad \text{6-12}$$

   where $\overline{M_0}$ is the mean of the AMFs of the pixels considered for computing $N_{s,0}$. There must be a sufficient number of observations in the reference sector to make this destriping reliable, especially due to the high level of noise in glyoxal retrievals. Note that the use of mean radiances as the DOAS reference (section 6.2.1) makes the application of this destriping step less critical.

2. Despite the destriping step, a residual broadband row-dependent structure in the slant columns has been identified at higher solar zenith angles (Figure 10 – left panel). Although the origin of this structure is not understood, we adapted the background correction to mitigate it[1]. Following a similar approach as in step 1, we bin all slant columns N'_s (and their corresponding AMFs) located in an extended reference sector (Latitudes in [40°S-40°N], longitudes in [165°E-220°E]) to compute correction factors in a two-dimension matrix as a function of the latitude *l* (from 40°S to 40°N, bin width: 20°) and row index *r* (from 1 to 450, bin width: 15) as

   $$C(r,l) = N'_{s,0}(r,l) - N_{v,0,ref} \times \overline{M_0(r,l)}, \qquad \text{6-13}$$

   Those correction factors are applied in two steps as

   $$N''_s(r,l) = N'_s(r,l) - (C(r,l) - mean(C, dim = r)) - mean(C, dim = r, l) \qquad \text{6-14}$$

   where *mean(C,dim=…)* indicates the dimension along which the averaging process is performed. This approach allows correcting for the residual row-dependent structure and for an overall possible bias, without significantly modifying the global latitudinal distribution of the background glyoxal columns, which is poorly known.

Figure 10 (right panel) shows the reduction of the residual row-dependent structure at Northern mid-latitudes. Figure 11 also illustrates this for one single orbit of that day. Mean glyoxal vertical columns of glyoxal are plotted as a function of the row index for pixels located in an equatorial latitude band and in a northern mid-latitude band. The three panels show results for different approaches: (a) No Background correction, (b) a latitude-independent background correction, (c) a latitude-dependent background correction as described before. The row-dependence of the uncorrected columns is different in the two

---

[1] An alternative approach to reduce such remaining SZA/latitude-dependent artifacts would be to use as reference spectra in the DOAS fit step some mean radiance spectra for each row computed in different latitude bands. In addition to the technical difficulties associated to this approach (a regular change of the reference spectrum during the along-track processing would be needed), there is also a risk of discontinuities appearing in the latitude dimension. A careful synchronization with the background-correction might mitigate this. A more fundamental limitation with this approach is that using latitude-binned reference radiance spectra would remove from the Pacific measurements all the information on the latitude dependence of the glyoxal concentrations, which would need to be reintroduced using external information from a model. As the glyoxal atmospheric content over the Pacific sector is poorly known, and even less its latitudinal dependence, this information is not available.

latitude bands (panel a), which leads to an overestimation of the mid-latitude columns if the row-dependent part correction relies on the equatorial measurements only (panel b). When the row-dependent correction depends also on the latitude, the residual structure at mid-latitudes is well reduced (panel c).

When computing the correction factors as described before, we only include observations passing the following filters in order to avoid outliers:

- Cloud fraction less than 0.2
- SZA<70°
- RMS < 2.e-3
- No snow/ice.

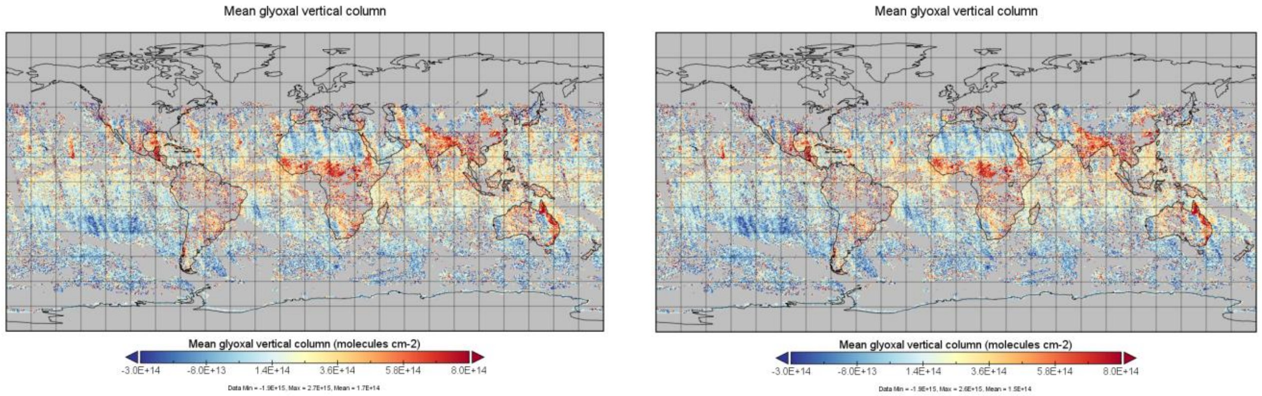

Figure 10: Mean glyoxal vertical columns (molec.cm^{-2}) measured by TROPOMI on 1st December 2018. (Left panel) The background correction does not include any SZA dependence and a systematic high bias is clearly visible for the nadir rows at Northern mid-latitudes. (Right panel) When the background correction includes such a latitudinal dependence, this bias is reduced.

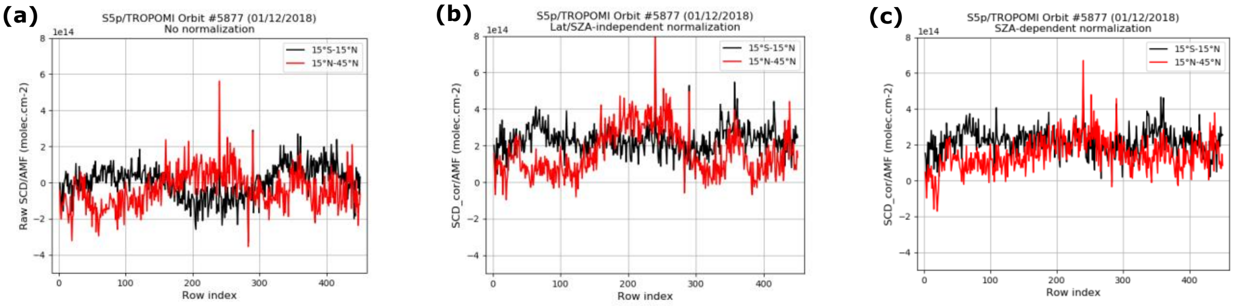

Figure 11: Row-dependence of the glyoxal vertical columns of orbit #5877 averaged in an equatorial latitude band and in a Northern mid-latitude band. (a) No background correction is applied; (b) a simple background correction without any latitudinal dependence is applied; (c) a latitude-dependent background correction is applied.

6.5 Error estimates and global budget

We present in this section how the different error components are estimated, as well as the resulting error budget when they are all combined.

The total uncertainty (accuracy and precision) on the glyoxal column products is composed of many sources of error. In part, those are related to the measuring instrument, such as uncertainties due to noise or knowledge of the slit function. In our DOAS-type algorithm, those instrumental errors propagate into the uncertainty on the slant column. Other types of error can be considered as model errors and are related to the representation of the observation physical properties that are not measured. Examples of model errors are uncertainties on the trace gas absorption cross-sections or on the a priori profile. Model errors can affect the slant column results or the air mass factor.

A formulation of the error can be derived analytically by error propagation, starting from the equation of the vertical column (6-1) which directly results from the different retrieval steps. As the main algorithm steps are performed independently, they are assumed to be uncorrelated. If we further assume normal probability distributions, the total error on the tropospheric vertical column can be expressed (Boersma et al., 2004; Lerot et al., 2010; De Smedt et al., 2008):

$$\sigma_{N_V}^2 = \frac{1}{M^2}\left({\sigma_{N_s}}^2 + \frac{(N_s - \overline{(N_{s,0} - N_{v,0,ref} \times M_0)})^2}{M^2}{\sigma_M}^2 + {\sigma_{N_{s,0}}}^2 + {N_{v,0,ref}}^2{\sigma_{M,0}}^2 + {M_0}^2{\sigma^2}_{N_{v,0,ref}}\right) \quad 6\text{-}15$$

where σ_{N_s}, σ_M and $\sigma_{N_{v,0,ref}}$ are the errors on the slant column, the air mass factor and the reference value used in the background correction, respectively. $\sigma_{N_{s,0}}$ and $\sigma_{M,0}$ represent the same errors but specifically for pixels belonging to the reference Pacific sector. The three last terms together represent the error associated to the background correction. A difficulty in the presented error formulation comes from the fact that it assumes the different error sources of the algorithm to be independent and uncorrelated, which is not strictly valid.

Another important point to note is that, in principle, systematic and random components of each given error source should be discriminated. If so, when deriving the error on the CHOCHO vertical column, each of the components of Eq. (6-15) can be written as:

$$\sigma_k^2 = \frac{\sigma_{k,rand}^2}{N} + \sigma_{k,syst}^2 \quad 6\text{-}16$$

where N is the number of ground pixels considered when averaging the observations. It is however very complicated to separate them in practice (see for example Boersma et al., 2004). Our approach is to qualify an error contribution as "random" if its impact on the column tends to average out in space and time. In practice, the propagation of the instrumental signal-to-noise in the L2 retrieval is considered as the main random error. For weak absorbers such glyoxal, this error component dominates for individual measurements and depends on the observation geometry, the scene reflectivity, and on the instrument itself. The other error components are considered as being systematic. It has however to be noted that the latter assumption may lead to conservative systematic error estimates and to an underestimation of the product scatter, depending on the time and spatial resolution of interest. In particular, uncertainties associated to the input parameters needed for the AMF calculation are directly related to the resolution of the used databases and may appear as random at coarser resolution. This has been discussed by Vigouroux et al. (2020) who attributed part of the scatter in formaldehyde vertical column TROPOMI/MAX-DOAS differences to a random component of the AMF errors.

The error analysis is complemented by the total column averaging kernel (A) formulation for DOAS-type retrievals (Eskes and Boersma, 2003):

$$A(p) = \frac{m(p)}{M} \quad 6\text{-}17$$

Column averaging kernels are particularly useful when comparing measured columns with e.g. model simulations or correlative validation data sets, because they allow removing the effect of the a priori profile shape information used in the retrieval (see Annex B).

6.5.1 Slant column errors

The retrieval noise for individual observations is limited by the SNR of TROPOMI measurements. A good estimate of the random variance of the reflectance (which results from the combined noise of radiance and irradiance measurements) is given by the reduced χ^2 of the fit, which is defined as the sum of squares (6-7) divided by the number of degrees of freedom in the fit (see also the Annex A). The covariance matrix Σ of the linear least squares parameter estimate is then given by:

$$\Sigma = \frac{\chi^2}{(k-n)}(J^T J)^{-1} \qquad 6\text{-}18$$

where k is the number of spectral pixels in the fitting interval, n is the number of fitted parameters and the matrix $J(j \times k)$ is formed by the absorption cross-sections. The diagonal elements of Σ represent $\sigma^2_{Ns,j,rand}$ of which the square root is the slant column error (SCD_e) of each absorber j. This term is computed by the DOAS module.

There are also systematic errors associated to the DOAS spectral fit, that are mainly dominated by slit function and wavelength calibration uncertainties, absorption cross-section uncertainties, by interferences with other species (O_4, liquid water, Ring, …), or by stray light corrections. Those contributions to the slant column errors are difficult to assess and can only be approximated from sensitivity tests (Lerot et al., 2010). In general, this term can be as high as 2–3×10^{14} molec.cm^{-2}. However, the use of a radiance as the DOAS fit reference and the application of the background correction removes a large part of the systematic error in the slant column fit. Therefore, we pragmatically estimate this remaining systematic slant column error $\sigma_{N_{s,syst}}$ to 1×10^{14} molec.cm^{-2}.

6.5.2 Air mass factor errors

The errors on the air mass factor depend on input parameter uncertainties and on the sensitivity of the air mass factor to each of them. This contribution is broken down into the squared sum (Boersma et al., 2004; Lerot et al., 2010; De Smedt et al., 2008):

$$\sigma^2_{M,syst} = \left(\frac{\partial M}{\partial A_s}\cdot\sigma_{A_s}\right)^2 + \left(\frac{\partial M}{\partial s}\cdot\sigma_s\right)^2 + (0.15M)^2 \qquad 6\text{-}19$$

where σ_{A_s}, σ_s are typical uncertainties on the surface albedo and profile shape, respectively. They are estimated from the literature or derived from comparisons with independent data.

The contribution of each parameter to the total air mass factor error depends on the observation conditions. The air mass factor sensitivities ($M' = \frac{\partial M}{\partial parameter}$), i.e. the air mass factor derivatives with respect to the different input parameters, can be derived for any particular condition of observation using the altitude-dependent AMF LUT, created with VLIDORT, and using the model profile shapes. In practice, a LUT of AMF sensitivities has been created using reduced grids from the AMF LUT and a parameterisation of the profile shapes.

A reasonable uncertainty on the albedo is $\sigma_{A_s} = 0.02$ (Kleipool et al., 2008). Using this value and the AMF sensitivity LUT allows to estimate for every pixel the first term of equation (6-19) and gives the AMF error component related to the surface reflectivity. Of course, in practice, more substantial errors can be introduced if the real albedo differs considerably from what is expected, for example in the case of the sudden snowfall or ice cover.

The uncertainty associated to the a priori profile shapes (the smoothing error) used in the retrieval are more difficult to assess, especially due to the scarcity of independent glyoxal profile measurements. Those errors are nevertheless large owing to the large uncertainty in our current knowledge of the glyoxal production mechanisms. To assess this error component and the sensitivity of the air mass factor to the profile shape, we have introduced one profile effective pressure s_p, i.e. the pressure below which resides 50% of the integrated glyoxal profile. $\frac{\partial M}{\partial s}$ is approached by $\frac{\partial M}{\partial s_p}$ and σ_s is taken equal to 50hPa. The latter value corresponds to the typical standard deviation of the model profile shape effective heights over polluted regions. Note that the error related to the a priori profiles can be removed with the use of the averaging kernels when comparing the satellite glyoxal columns to independent glyoxal profile measurements from models or MAX-

DOAS (see Annex B). That is the reason why an estimate of the total systematic error without this smoothing error is also provided in the L2 product:

$$\sigma^2_{M,syst,kernel} = \left(\frac{\partial M}{\partial A_s} \cdot \sigma_{A_s}\right)^2 + (0.15M)^2 \qquad \text{6-20}$$

The third term in equation (6-19) accounts for possible error in the AMF model itself (e.g. wavelength dependence, neglect of aerosols,…) and is estimated to be 15% of the air mass factor (Lorente et al., 2017).

As explained before, there is no cloud correction applied to compute the AMFs. Therefore, it is highly recommended to apply a stringent filter based on the cloud fraction (<20%) on the retrieved glyoxal vertical columns. Nevertheless, even with such a filter, an error on the AMF caused by residual cloud contamination may remain. This error, which strongly depends on the cloud coverage and altitude, is expected to average out in space and/or time when combining several observations. To consider this, we add a small random contribution to the air mass factor as

$$\sigma^2_{M,rand} = (0.05M)^2 \qquad \text{6-21}$$

6.5.3 Background correction error

Although the background correction is designed to overcome systematic features/deficiencies of the slant column fitting, some errors are also associated to this procedure. In particular, systematic errors on the reference slant columns and their air mass factors are propagated to the computed correction values. Also there is an uncertainty related to the used reference value of the glyoxal vertical column in the reference sector $N_{v,0,ref}$. Considering these different components, the background correction error can be estimated as

$$\sigma^2_{bck} = \frac{1}{M^2}\left(\sigma_{N_{s,0}}{}^2 + N_{v,0,ref}{}^2\sigma_{M,0}{}^2 + M_0{}^2\sigma_{N_{v,0,ref}}{}^2\right) \qquad \text{6-22}$$

where $\sigma_{N_{s,0}}$ is the systematic slant column error fixed to 1x10^{14} molec/cm² (see section 6.5.1), M_0 and $\sigma_{M,0}$ are the air mass factors and associated systematic errors in the reference sector. In practice, those quantities are treated similarly as the reference slant columns (i.e. binned in SZA and row bins – see section 6.4). $\sigma_{N_{v,0,ref}}$ represents the error associated to the reference value $N_{v,0,ref}$ and is fixed to 5x10^{13} molec/cm².

6.5.4 Global budget: Total precision and trueness

Combining the different error components discussed above, the total random error (or precision) is computed as

$$\sigma^2_{Nv,rand} = \frac{\sigma^2_{Ns,rand} + \sigma^2_{M,rand} N_v^2}{M^2} \qquad \text{6-23}$$

The instrumental signal-to-noise ratio is the main factor introducing random errors in the product. The TROPOMI instrument has a signal-to-noise ratio around 1600 in the visible spectral range for low albedo scenes. **Error! Reference source not found.** Figure 12 (d) illustrates the glyoxal VCD precision estimates for one day of TROPOMI observations (1st June 2018). This precision is generally less than 0.8-1x10^{15} molec/cm² over dark surfaces and much lower for bright surfaces (clouds and snow-covered scenes). Previous studies (Alvarado et al., 2014; Chan Miller et al., 2014; Lerot et al., 2010) have shown that this precision is slightly larger for the older instruments GOME-2 and OMI (in the range 1-1.5 x 10^{15} molec/cm²). A specific requirement for the random error has only been defined for the Sentinel-5 mission (<1.5x10^{15} molecules.cm^{-2} – see Table 1), which appears to be met for most of TROPOMI observations. For individual satellite ground pixels, the random error is the dominant source of error on the total vertical column. This clearly points to the importance of the spatial/temporal averages, which reduce the random error by the square root of the number of observations and facilitate the detection of meaningful glyoxal signal.

The total systematic error (trueness) is computed as

$$\sigma^2_{Nv,syst} = \sigma^2_{bck} + \frac{\sigma^2_{Ns,syst}}{M^2} + \frac{\sigma^2_{M,syst} \times N_v^2}{M^2} \qquad \text{6-24}$$

Similarly, the total systematic error without the smoothing error component is calculated as

$$\sigma^2_{Nv,kernel,syst} = \sigma^2_{bck} + \frac{\sigma^2_{Ns,syst}}{M^2} + \frac{\sigma^2_{M,kernel,syst} \times N_v^2}{M^2} \qquad \text{6-25}$$

Note that the conversion of the AMF error into an absolute vertical column error (3rd terms of the two equations above) requires this error to be multiplied by the corresponding vertical column. Because of the high level of noise in the product, using the retrieved column for this would lead to a strong overestimation of the systematic error. To circumvent this, we use instead pre-computed climatological glyoxal noise-free VCDs. Figure 12 shows the mean estimates of the glyoxal VCD trueness for the month of June 2018, which are generally in the range 1-3x10^{14} molec/cm²(20-60% for emission regimes). Note that pixels strongly contaminated by clouds (cloud fraction > 20%) or covered by snow/ice have been discarded. Systematic errors are expected to be larger for those pixels as spectral interferences are larger (see section 6.3.3) and the information content becomes limited (cloud shielding effect). Figure 12 also shows mean AMFs for June 2018. Small AMFs are generally caused by a priori profiles peaking near the surface, which makes the retrieval more sensitive to albedo uncertainties and to a lesser extent to the a priori profile shape uncertainties. This explains the anti-correlation between the AMF and the systematic errors. On contrary, large AMFs are caused either by bright surface or by background a priori profiles. For such cases, retrieval systematic errors are smaller. In general, those systematic error estimates are close to the requirements as discussed in section 5.3.

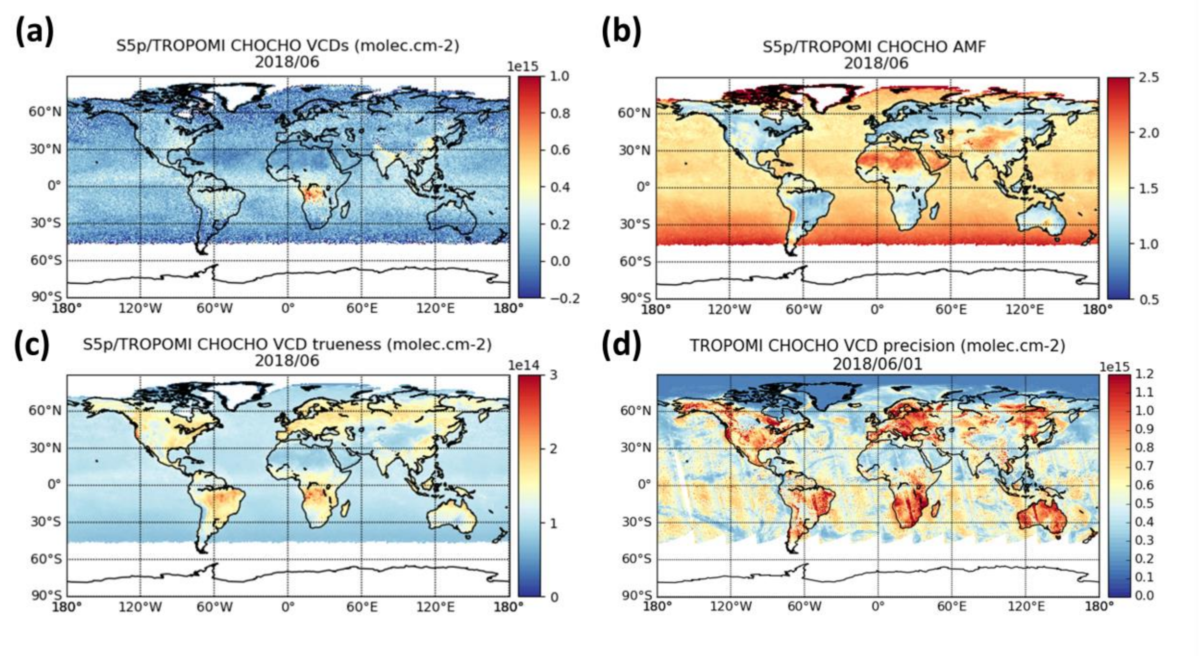

Figure 12: (a) TROPOMI June 2018 monthly means of glyoxal tropospheric columns, glyoxal air mass factors (panel (b)) and glyoxal tropospheric column systematic errors (panel (c)). Scenes contaminated by clouds or Ice/snow have been filtered out. Panel (d) shows glyoxal tropospheric column random errors for one single day, in which all observations have been kept to illustrate the impact of the scene brightness.

6.5.5 Quality Assurance Values

All variables contained in the L2 files are provided for all TROPOMI observations with a solar zenith angle less than 75°. No filter is applied by default for degraded fit quality, cloud or aerosol contamination, snow/ice cover… Instead, the user is recommended to use the *qa_value* variable to filter out the data. The quality assurance value is a numerical value in the range [0 1], with the convention that a value <0.5 means that the pixel retrieval result is recommended to be discarded. **Keeping data with a qa_value equal or higher than 0.5** guarantees that only clear sky observations (cloud fraction less or equal to 20%), not covered by snow/ice and with good fit quality are considered. This approach allows advanced users to implement their own filtering approach by making use of the different variables contained in the files. It is however reminded that no cloud correction is applied for the AMF computation. It is therefore essential to reject cloud-contaminated pixels, even if there is some flexibility on the cloud fraction thresholds to be used for this.

A qa_value is assigned to every observation. They are computed with a very simple scheme consisting in subtracting delta values from the initial value 1 for each of the fulfilled conditions listed in the following table.

Description	qa_value	Comment
Solar zenith angle out of range error (SZA>85)	set to 0	
Solar zenith angle out of range filter (70<SZA>85)	qa_value - (0.8-cos(SZA))	only for SZA>=70 ; SZA in radians
High liquid water signal (Ns,lw >0.01)	qa_value – 0.2	
High liquid water signal over lands (Ns,lw >0.002 and land flag =1)	qa_value – 0.51	
Cloud filtering	qa_value - f_c x 2.5	qa_value reduced only for f_c >0.2
Snow/ice flag	qa_value – 0.51	
Low AMF (AMF<0.3)	qa_value – 0.51	
Poor fit quality (RMS>2E-3)	qa_value – 0.51	
qa_value < 0	set to 0	

7 Feasibility

7.1 Estimated Computational Effort

The TROPOMI instrument samples the Earth's surface in the visible spectral range with a spatial resolution of 3.5x7km² and 3.5x5.5km² before and after August 2019, respectively. This gives about 1.500.000 or 1.900.000 spectra recorded per orbit in the channel 4 of the instrument. Table 4 gives an estimate of the processing time needed by each of the glyoxal algorithm modules to process one day of TROPOMI observations. Each of those modules actually handle each orbit separately except the background correction module, which treats all orbit of the day simultaneously. Those numbers have been obtained using one single Intel Xeon E5-2680V3 CPU. Only a fraction of the pixels per orbit are processed as there is a upper limit in SZA at 75°. On average, the entire processing time required to process one S5P orbit is about 40 minutes. The fit of the slant column is by far the most time consuming part of the algorithm. Due to the large amount of TROPOMI observations, some of the module require several GB of RAM (e.g. up to 10 GB for the DOAS module).

Table 4: Time needed by each of the modules of the BIRA CHOCHO scientific algorithm to process one day of TROPOMI observations..

	Time per day of TROPOMI observations (14 orbits with 1,900,000 pixels	Prototype software/Language
Slant column (1 fitting window + spike removal algorithm)	14 x 25 min	QDOAS v3.4.3 (C/C++)
AMF (LUT) + Error estimate	14 x 7 min	Python
Normalization + Error estimate	15 min	Python
Various data transfer + Format preparation	14 x 5 min	Bash/Python
Total	< 540 min (9h) < 40 min per orbit	

7.2 Inputs

There is a number of input data needed for retrieving glyoxal tropospheric columns from TROPOMI observations, both static and dynamic, which are summarized in Table 5 and Table 6.

Main input data sets have been discussed in section 6. The static data include spectroscopic data, topography, ground reflectivity, a priori information on vertical distribution of glyoxal concentrations, as well as the Box-AMF LUT generated internally. As for the dynamic data, L1b spectral data in the visible spectral range, along with their geolocalisation, are obviously needed. Other dynamic inputs are required for filtering purposes. In particular, filters are currently applied to remove cloud- and/or snow-contaminated scenes. Also a land classification flag helps to discriminate land and ocean pixels for the selection of the a priori glyoxal profile. Those different flags are currently extracted from the NO_2 operational product. More details on the format of the input auxiliary data and extracted variables are given in the Auxiliary User Manual [AD03].

7.2.1 Static Inputs

Table 5: List of static auxiliary input needs for generating the glyoxal VCD product.

Parameter	Physical unit	Source
High-resolution solar spectrum	mol s^{-1} m^{-2} nm^{-1}	Chance and Kurucz (2010)
Absorption O_3 cross-sections at 223 K	cm^{2}molec.$^{-1}$	Serdyuchenko et al. (2014)
Absorption NO_2 cross-section at 220 and 296 K	cm^{2}molec.$^{-1}$	Vandaele et al. (1998)
Absorption glyoxal cross-section at 296K	cm^{2}molec.$^{-1}$	Volkamer et al. (2005)
Absorption water vapor cross-section at 293K	cm^{2}molec.$^{-1}$	Rothman et al. (2013)
Absorption O_4 cross-section at 293K	cm^{5}molec.$^{-2}$	Thalman and Volkamer (2013)
Liquid water absorption cross-section	m^{-1}	Mason et al. (2016)
Ring cross-section	1	Generated internally
Two scene heterogeneity cross-sections	1	Generated internally
Common residual cross-section	1	Generated internally
Surface Albedo in the fitting window	1	Kleipool et al. (2008)
Surface altitude	m	GMTED 2010, Danielson and Gesch (2011)
A-priori CHOCHO vertical profile shapes	1 (vmr)	CTM MAGRITTE TORERO profile over oceans (Volkamer et al., 2015)
Look-up table of altitude-resolved AMFs and AMF Jacobians	1	Generated internally with VLIDORT

7.2.2 Dynamic Inputs

Table 6: List of dynamic auxiliary input needs for generating the glyoxal VCD product.

Parameter	Physical unit	Source
Radiance	mol s^{-1} m^{-2} nm^{-1} sr^{-1}	S5p L1b radiance product (Band 4)
Small pixel radiance	mol s^{-1} m^{-2} nm^{-1} sr^{-1}	S5p L1b radiance product (Band 4)
Irradiance	mol s^{-1} m^{-2} nm^{-1}	S5p L1b irradiance product (UVN)
Latitude center	degrees	S5p L1b radiance product (Band 4)
Longitude center	degrees	S5p L1b radiance product (Band 4)
Latitude corner	degrees	S5p L1b radiance product (Band 4)
Longitude corner	degrees	S5p L1b radiance product (Band 4)
SZA (at pixel center)	degrees	S5p L1b radiance product (Band 4)

VZA (at pixel center)	degrees	S5p L1b radiance product (Band 4)
SAA (at pixel center)	degrees	S5p L1b radiance product (Band 4)
VAA (at pixel center)	degrees	S5p L1b radiance product (Band 4)
Surface altitude	m	S5p operational NO2 product
Cloud fraction	1	S5p operational NO2 product
Snow/ice flag	1	S5p operational NO2 product
Land classification flag	1	S5p operational NO2 product

7.3 Output Product Overview

The current output format of the L2 CHOCHO files produced by this scientific algorithm follows closely the current conventions of the operational products, in terms of filename and content structure as well as variable name nomenclature and units. The output files are in NetCDF-4, with the convention CF.

A typical L2 glyoxal filename is structured as:

S5P_OFFL_L2__CHOCHO___20180904T054104_20180904T072234_04623_01_010000_20190315.nc

where the two first time stamps in yellow correspond to start and end of the orbit, the orbit number is in green, the grey substrings inherit from the collection and product versions of the L1 data, and the creation date is in cyan.

Every individual L2 file corresponds to one S5p orbit and include for each ground pixel a comprehensive list of variables, covering:

- glyoxal vertical column, slant column and air mass factor
- measurement time and geolocation (center and corner), taken from the L1b product
- retrieval diagnostics including error estimates, averaging kernel and a priori information.
- quality flags.
- input parameters
- Various flags useful for using the product.

Following the operational products, all variables provided in the L2 glyoxal files are organized in the structure sketched as in Figure 13. Detailed information can be found in the Product User Manual [AD05].

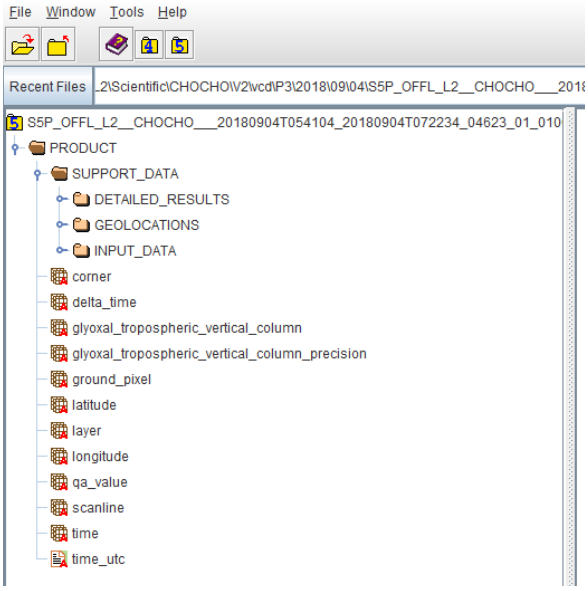

```
_2\Scientific\CHOCHO\V2\vcd\P3\2018\09\04\S5P_OFFL_L2__CHOCHO___2018
S5P_OFFL_L2__CHOCHO___20180904T054104_20180904T072234_04623_01_010
PRODUCT
  SUPPORT_DATA
    DETAILED_RESULTS
    GEOLOCATIONS
    INPUT_DATA
  corner
  delta_time
  glyoxal_tropospheric_vertical_column
  glyoxal_tropospheric_vertical_column_precision
  ground_pixel
  latitude
  layer
  longitude
  qa_value
  scanline
  time
  time_utc
```

Figure 13 : L2 glyoxal file structure

Table 7 gives the current list of variables provided in the L2 glyoxal column files. Note that the current size of each L2 file is about 600MB.

Table 7 : List of variables that are currently included in the TROPOMI glyoxal product. The second column indicates the GROUP of the file content structure in which the variable is stored.

Name	Group	Unit	Description / long name
time	PRODUCT	s	Reference time of the measurements.
scanline	PRODUCT	-	Coordinate variable defining the indices along track.
delta_time	PRODUCT	ms [since time]	Time difference with reference time for each scanline.
ground_pixel	PRODUCT	-	Coordinate variable defining the indices across track.
glyoxal_tropospheric_vertical_column	PRODUCT	mol.m^{-2}	Glyoxal tropospheric column
glyoxal_tropospheric_vertical_column_precision	PRODUCT	mol.m^{-2}	Glyoxal tropospheric column random error
qa_value	PRODUCT	1	Quality assurance value describing the quality of the product
latitude	PRODUCT	degree north	Latitude of the center of each ground pixel
longitude	PRODUCT	degree east	Longitude of the center of each ground pixel
fitted_slant_columns	DETAILED_RESULTS	Various	Slant column density from all absorbers in the fitting window
fitted_slant_columns_precision	DETAILED_RESULTS	Various	Slant column density random errors from all absorbers in the fitting window
fitted_radiance_shift	DETAILED_RESULTS	nm	Wavelength shift from the DOAS fit
fitted_radiance_stretch	DETAILED_RESULTS	1	Wavelength stretch from the DOAS fit
fitted_root_mean_square	DETAILED_RESULTS	1	DOAS fit residuals
glyoxal_slant_column_corrected	DETAILED_RESULTS	mol.m^{-2}	Normalized glyoxal slant column
glyoxal_slant_column_corrected_trueness		mol.m^{-2}	Systematic error on the glyoxal slant column
glyoxal_tropospheric_air_mass_factor	DETAILED_RESULTS	1	Clear air mass factor
glyoxal_ tropospheric_air_mass_factor_trueness	DETAILED_RESULTS	1	Systematic error on the air mass factor
glyoxal_tropospheric_air_mass_factor_kernel_trueness	DETAILED_RESULTS	1	Systematic error on the air mass factor without smoothing error
glyoxal_tropospheric_air_mass_factor_precision	DETAILED_RESULTS	1	Random error on the air mass factor
glyoxal_tropospheric_vertical_column_trueness	DETAILED_RESULTS	mol.m^{-2}	Glyoxal tropospheric column systematic error
glyoxal_tropospheric_vertical_column_kernel_trueness	DETAILED_RESULTS	mol.m^{-2}	Glyoxal tropospheric column systematic error without smoothing error
scene_inhomogeneity_factor	DETAILED_RESULTS	1	Degree of the scene brightness heterogeneity (0 : homogeneous ; -1/+1 maximum heterogeneity).

averaging_kernel	DETAILED_RESULTS	1	Averaging kernel
glyoxal_profile_apriori	DETAILED_RESULTS	1 (vmr)	A priori glyoxal profile
glyoxal_profile_apriori_pressure	DETAILED_RESULTS	Pa	Pressure grid of a priori glyoxal profile
solar_zenith_angle	GEOLOCATIONS	degree	Zenith angle of the sun measured from the ground pixel location
solar_azimuth_angle	GEOLOCATIONS	degree	Azimuth angle of the sun measured from the ground pixel location
viewing_zenith_angle	GEOLOCATIONS	degree	Zenith angle of the satellite measured from the ground pixel location
viewing_azimuth_angle	GEOLOCATIONS	degree	Azimuth angle of the satellite measured from the ground pixel location
latitude_bounds	GEOLOCATIONS	degree north	The four latitude boundaries of each ground pixel.
longitude_bounds	GEOLOCATIONS	degree east	The four longitude boundaries of each ground pixel.
surface_pressure	INPUT_DATA	Pa	Surface pressure from the CTM adjusted for surface elevation.
surface_altitude	INPUT_DATA	m	Height of the surface averaged over the ground pixel.
land_ocean_flag	INPUT_DATA	1	Indicates whether the gorund_pixel is located over land or ocean
snow_ice_flag	INPUT_DATA	1	Surface condition (snow/ice)
surface_classification	INPUT_DATA	1	Surface classification
surface_albedo	INPUT_DATA	1	Surface albedo
cloud_fraction_crb	INPUT_DATA	1	Cloud fraction
cloud_pressure_crb	INPUT_DATA	Pa	Cloud fraction
aerosol_index_354_388	INPUT_DATA	1	Aerosol absorbing index 354/388 pair
glyoxal_reference_sector_mean_scd	INPUT_DATA/BACKGROUND_CORRECTION	mol.m^{-2}	Mean glyoxal slant columns of pixels falling into the reference sector
glyoxal_reference_sector_mean_model_scd	INPUT_DATA/BACKGROUND_CORRECTION	mol.m^{-2}	Mean simulated glyoxal slant columns of pixels falling into the reference sector
glyoxal_reference_sector_mean_air_mass_factor	INPUT_DATA/BACKGROUND_CORRECTION	1	Mean glyoxal AMF for the pixels falling into the reference sector
glyoxal_reference_sector_mean_air_mass_factor_trueness	INPUT_DATA/BACKGROUND_CORRECTION	1	Mean glyoxal AMF systematic error for the pixels falling into the reference sector

number_of_reference_sector_mean_obs [‡]	INPUT_DATA/BACKGROUND_CORRECTION	1	Number of pixels considered for the latitude/ground_pixel binning of the reference sector.

8 Validation

As for other tropospheric data products, the validation of satellite glyoxal column measurements is difficult and challenging. Ideally, we need to have long-term time series of independent reference glyoxal measurements covering several seasons and at different locations worldwide representative of various geophysical conditions and emission regimes. As addressed before, the use of uncertain a priori information on the glyoxal vertical distribution may lead to significant uncertainties. Having independent information on this distribution would be certainly valuable.

However, the availability of such reference data is very limited and retrievals from the ground suffer from the same limitations as from space, i.e. high sensitivity to spectral interferences and sensitivity to noise, which make this activity very challenging. In addition, the retrieval strategy across the ground-based network is far to be homogenized, leading to inter-stations discrepancies. To mitigate this, comparisons are also performed with glyoxal columns retrieved from other algorithms and/or satellites.

A summary of the validation results of the S5p glyoxal product as obtained during the study is given in this section. For an in-depth discussion of the validation results, the reader is invited to read the Product Validation Report [AD04] or Lerot et al. (2021).

8.1 Ground-based validation

We have identified a series of glyoxal reference MAX-DOAS measurement data sets from nine stations located in Asia and Europe that are used in this study (see [AD03] and [AD04]). Such measurements provide mainly glyoxal tropospheric columns. In theory, they offer the potential to gain limited information on vertical distribution (e.g. surface concentration in addition to the tropospheric column) but in practice, this is only available for the stations operated by BIRA-IASB in Uccle (Belgium) and Xianghe (China).

Figure 14 compares the glyoxal tropospheric column seasonal cyle from TROPOMI and the MAX-DOAS at the nine considered stations. More details can be found in the validation report [AD04] but the main conclusions of the exercise are:

- The seasonal cycles observed from TROPOMI agree very well with the MAX-DOAS cycles. Correlation coefficients are generally high and range between 0.61 and 0.87, except in Bremen where the correlation is poor.
- The absolute values of the glyoxal columns from TROPOMI and the MAX-DOAS are also consistent with overall biases less than 1×10^{14} molec/cm² for stations with moderate columns. The bias is however significantly higher in Phimai/Thailand and Pantnagar/india. The origin of this bias is not fully understood. It may be caused by local extreme conditions (e.g. strong contamination by aerosols). In addition, the MAX-DOAS columns at those stations are very high and it is not uncommon to have such biases in UV-Visible satellite retrievals for strongly polluted sites. It cannot be excluded that part of the bias originates from the MAX-DOAS retrieval strategy at those sites, especially since such a bias is not identified at another Indian station (Mohali).
- There are indications that the TROPOMI glyoxal columns are low biased during winter at mid-latitudes.
- The scatter of the TROPOMI/MAX-DOAS differences and the correlation coefficients were improved with respect to other satellite instruments, which points to the better performance of TROPOMI for the detection of glyoxal from space due to the higher signal-to-noise ratio of the spectral measurements and the large amount of available data.

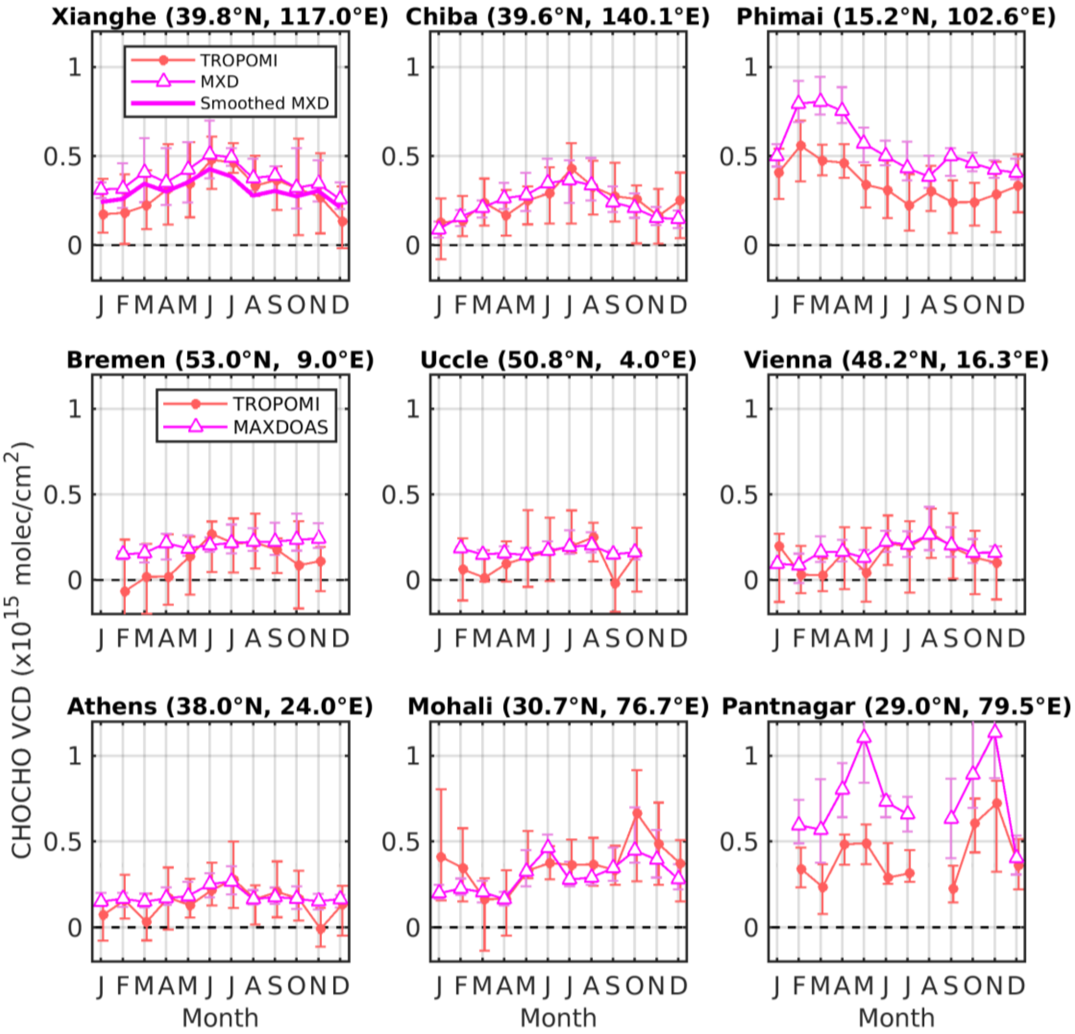

Figure 14: Comparison of the monthly median glyoxal tropospheric vertical column seasonal cycle as retrieved from TROPOMI and MXD at the nine stations considered during the study. In Xianghe, MAX-DOAS data smoothed with the satellite averaging kernels are also shown. The error bars represent the interannual variability (25% and 75% percentiles based on the full time series available).

8.2 Comparisons with other satellite data sets

Inter-satellite comparisons of glyoxal products are also important to assess their consistency and to verify that they can be combined together for specific studies (e.g. long-term trend analysis). Two types of comparison may provide complementary information:

- Comparisons with glyoxal products from other satellites (OMI, GOME-2A/B) generated with a similar algorithm as that applied to TROPOMI will provide information on possible differences related to instrumental characteristics.
- Comparison with the IUP-Bremen TROPOMI (Alvarado et al., 2014, 2019) will give insight in differences originating from the algorithms themselves.

Figure 15 compares seasonal maps as derived from many years of GOME-2A, GOME-2B, OMI and TROPOMI glyoxal tropospheric column measurements based on consistent algorithmic baselines. The general patterns of the glyoxal tropospheric column fields and their seasonal variability as observed by all instruments are very consistent with each others. The seasonal glyoxal variability is mostly related to the seasonal (temperature) dependence of biogenic emissions, but also to the high variability of fire events. For example, in the TROPOMI maps, a larger glyoxal signal is observed in Dec-Jan-Feb along the Eastern Australian coast, caused by the huge fires that occurred in January 2020. In addition, as the TROPOMI data set is shorter, individual exceptional events are more visible than when combining more years of observations.

Figure 16 presents a comparison of the mean glyoxal column seasonal cycles derived from TROPOMI, OMI, GOME-2A and GOME-2B in a few regions worldwide. In general, they all agree very well both in terms of variability and of absolute values. Based on a comparison in many different regions worldwide, it has been estimated that the inter-satellite deviations are generally less than 5×10^{13} molec/cm² (20%). This demonstrates that glyoxal retrievals respond in the same manner to our selection of settings for all nadir-viewing satellite instruments.

In conclusion, those validation results, relying on comparisons with glyoxal measurements from independent ground-based and space instruments, give confidence into the compliance with the defined scientific product requirements discussed in section 5.3. Indeed, the estimated TROPOMI/MAX-DOAS biases are generally less than the defined threshold of 2.5×10^{14} molec.cm^{-2} or 50% (least stringent). In Pantnagar, the bias is nevertheless larger and is not fully understood. It has to be reminded that independent ground-based measurements are sparse and cover a limited range of geophysical conditions. Therefore, it cannot be guaranteed that those requirements are met in all conditions. For example, it is expected that larger errors would occur in case of large aerosol loads, due to the unaccounted impact on the radiative transfer but also (and mostly in the case a low absorber such as glyoxal) to local larger biases due to spectral interferences with O4 and/or Ring spectral signatures. Sensitivity tests based on synthetic spectra realized in the framework of the Sentinel-4 baseline algorithm preparation have shown that, while the retrieved columns are close to true values for atmosphere clear of cloud/aerosols, the deviations can be significantly larger for more complicated scenarios [RD11].

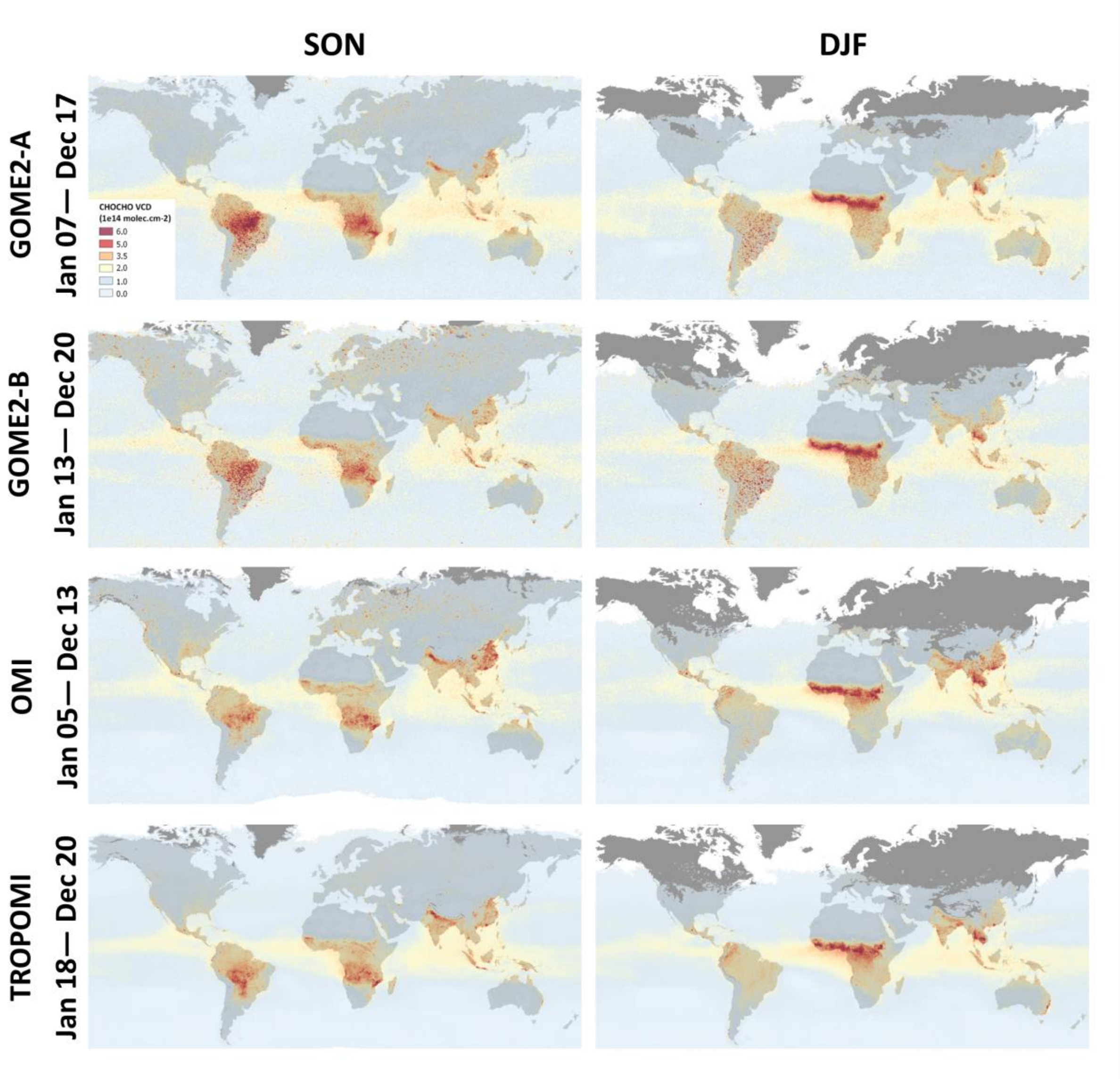

Figure 15: Comparison of long-term averaged global CHOCHO VCDs (in 1014 molec/cm^2) derived from GOME-2A, GOME-2B, OMI and TROPOMI sensors, for the September-October-November period (left panels) and the December-January-February period (right panels).

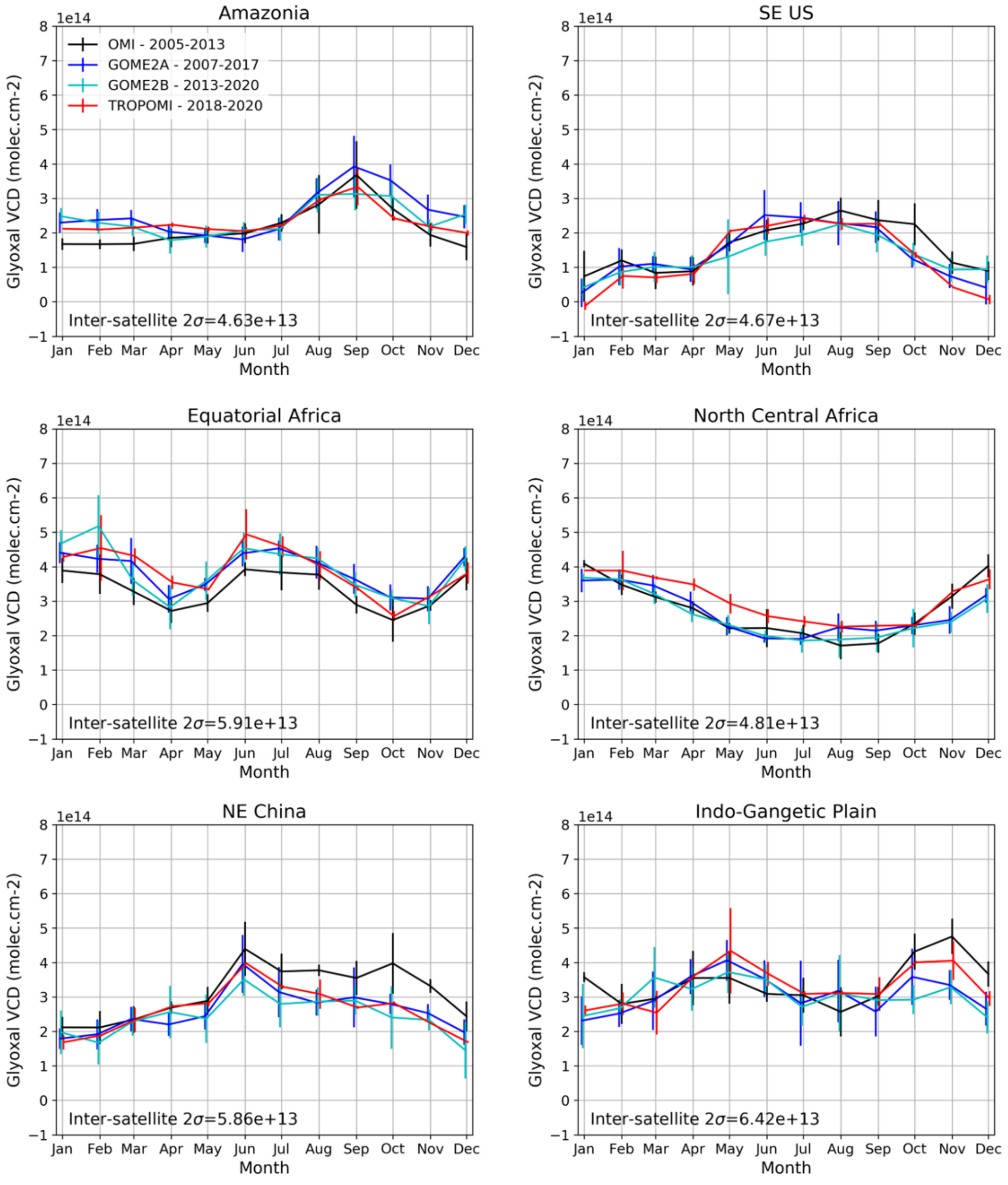

Figure 16: Comparison of the climatological seasonal variation of the monthly median glyoxal VCDs from GOME-2A/B, OMI and TROPOMI in a few selected regions worldwide. The error bars represent the interannual variability as derived from the full time series.

9 References

Alvarado, L. M. A., Richter, A., Vrekoussis, M., Wittrock, F., Hilboll, A., Schreier, S. F. and Burrows, J. P.: An improved glyoxal retrieval from OMI measurements, Atmos. Meas. Tech., 7(12), 4133–4150, doi:10.5194/amt-7-4133-2014, 2014.

Alvarado, L. M. A., Richter, A., Vrekoussis, M., Hilboll, A., Kalisz Hedegaard, A. B., Schneising, O. and Burrows, J. P.: Unexpected long-range transport of glyoxal and formaldehyde observed from the Copernicus Sentinel-5 Precursor satellite during the 2018 Canadian wildfires, Atmos. Chem. Phys. Discuss., 1–22, doi:10.5194/acp-2019-684, 2019.

Anand, J. S., Monks, P. S. and Leigh, R. J.: An improved retrieval of tropospheric NO $_2$ from space over polluted regions using an Earth radiance reference, Atmos. Meas. Tech., 8(3), 1519–1535, doi:10.5194/amt-8-1519-2015, 2015.

Bauwens, M., Stavrakou, T., Müller, J.-F., De Smedt, I., Van Roozendael, M., van der Werf, G. R., Wiedinmyer, C., Kaiser, J. W., Sindelarova, K. and Guenther, A.: Nine years of global hydrocarbon emissions based on source inversion of OMI formaldehyde observations, Atmos. Chem. Phys., 16(15), 10133–10158, doi:10.5194/acp-16-10133-2016, 2016.

Boersma, K. F., Eskes, H. J. and Brinksma, E. J.: Error analysis for tropospheric NO $_2$ retrieval from space, J. Geophys. Res. Atmos., 109(D4), n/a-n/a, doi:10.1029/2003JD003962, 2004.

Boersma, K. F., Eskes, H. J., Dirksen, R. J., van der A, R. J., Veefkind, J. P., Stammes, P., Huijnen, V., Kleipool, Q. L., Sneep, M., Claas, J., Leitão, J., Richter, A., Zhou, Y. and Brunner, D.: An improved tropospheric NO $_2$ column retrieval algorithm for the Ozone Monitoring Instrument, Atmos. Meas. Tech., 4(9), 1905–1928, doi:10.5194/amt-4-1905-2011, 2011.

Chan Miller, C., Gonzalez Abad, G., Wang, H., Liu, X., Kurosu, T., Jacob, D. J. and Chance, K.: Glyoxal retrieval from the Ozone Monitoring Instrument, Atmos. Meas. Tech., 7(11), 3891–3907, doi:10.5194/amt-7-3891-2014, 2014.

Chan Miller, C., Jacob, D. J., González Abad, G. and Chance, K.: Hotspot of glyoxal over the Pearl River delta seen from the OMI satellite instrument: implications for emissions of aromatic hydrocarbons, Atmos. Chem. Phys., 16(7), 4631–4639, doi:10.5194/acp-16-4631-2016, 2016.

Chance, K. and Kurucz, R. L.: An improved high-resolution solar reference spectrum for earth's atmosphere measurements in the ultraviolet, visible, and near infrared, J. Quant. Spectrosc. Radiat. Transf., 111(9), 1289–1295, doi:10.1016/j.jqsrt.2010.01.036, 2010.

Chance, K. V. and Spurr, R. J. D.: Ring effect studies: Rayleigh scattering, including molecular parameters for rotational Raman scattering, and the Fraunhofer spectrum, Appl. Opt., 36(21), 5224, doi:10.1364/ao.36.005224, 1997.

Coburn, S., Ortega, I., Thalman, R., Blomquist, B., Fairall, C. W. and Volkamer, R.: Measurements of diurnal variations and eddy covariance (EC) fluxes of glyoxal in the tropical marine boundary layer: description of the Fast LED-CE-DOAS instrument, Atmos. Meas. Tech. Discuss., 7(10), 6245–6285, doi:10.5194/amt-7-3579-2014, 2014.

Danckaert, T., Fayt, C., van Roozendael, M., De Smedt, I., Letocard, V., Merlaud, A. and Pinardi, G.: QDOAS software user manual. [online] Available from: http://uv-vis.aeronomie.be/software/QDOAS/QDOAS_manual.pdf, 2017.

Danielson, J. J. and Gesch, D. B.: Global multi-resolution terrain elevation data 2010 (GMTED2010)., 2011.

DiGangi, J. P., Henry, S. B., Kammrath, A., Boyle, E. S., Kaser, L., Schnitzhofer, R., Graus, M., Turnipseed, A., Weber, R. J., Hornbrook, R. S., Cantrell, C. A., Maudlin, R. L., Kim, S., Nakashima, Y., Wolfe, G. M., Kajii, Y., Apel, E. C. C., Goldstein, A. H., Guenther, A., Karl, T., Hansel, A., Keutsch, F. N., Park, J.-H. J.-H., Weber, R. J., Hornbrook, R. S., Cantrell, C. A., Maudlin III, R. L., Kim, S., Nakashima, Y., Wolfe, G. M., Kajii, Y., Apel, E. C. C., Goldstein, A. H., Guenther, A., Karl, T., Hansel, A. and Keutsch, F. N.: Observations of glyoxal and formaldehyde as metrics for the anthropogenic impact on rural photochemistry, Atmos. Chem. Phys., 12(20), 9529–9543, doi:10.5194/acp-12-9529-2012, 2012.

Eskes, H. J. and Boersma, K. F.: Averaging kernels for DOAS total-column satellite retrievals, Atmos. Chem. Phys., 3(5), 1285–1291, doi:10.5194/acp-3-1285-2003, 2003.

Fu, T.-M. T.-M., Jacob, D. J., Wittrock, F., Burrows, J. P., Vrekoussis, M. and Henze, D. K.: Global budgets of atmospheric glyoxal and methylglyoxal, and implications for formation of secondary organic aerosols, J. Geophys. Res., 113(D15), D15303, doi:10.1029/2007JD009505, 2008.

Grainger, J. F. and Ring, J.: Anomalous fraunhofer line profiles, Nature, 193(4817), 762, doi:10.1038/193762a0, 1962.

Heckel, A., Kim, S.-W., Frost, G. J., Richter, A., Trainer, M. and Burrows, J. P.: Influence of low spatial resolution a priori data on tropospheric NO_2 satellite retrievals, Atmos. Meas. Tech., 4(9), 1805–1820, doi:10.5194/amt-4-1805-2011, 2011.

Kaiser, J., Wolfe, G. M., Min, K. E., Brown, S. S., Miller, C. C., Jacob, D. J., deGouw, J. A., Graus, M., Hanisco, T. F., Holloway, J., Peischl, J., Pollack, I. B., Ryerson, T. B., Warneke, C., Washenfelder, R. A. and Keutsch, F. N.: Reassessing the ratio of glyoxal to formaldehyde as an indicator of hydrocarbon precursor speciation, Atmos. Chem. Phys., 15(13), 7571–7583, doi:10.5194/acp-15-7571-2015, 2015.

Kleipool, Q. L., Dobber, M. R., de Haan, J. F. and Levelt, P. F.: Earth surface reflectance climatology from 3 years of OMI data, J. Geophys. Res., 113(D18), D18308, doi:10.1029/2008JD010290, 2008.

Lawson, S. J., Selleck, P. W., Galbally, I. E., Keywood, M. D., Harvey, M. J., Lerot, C., Helmig, D. and Ristovski, Z.: Seasonal in situ observations of glyoxal and methylglyoxal over the temperate oceans of the Southern Hemisphere, Atmos. Chem. Phys., 15(1), 223–240, doi:10.5194/acp-15-223-2015, 2015.

Lerot, C., Stavrakou, T., De Smedt, I., Müller, J. F., Van Roozendael, M., M¨uller, J. F. and Van Roozendael, M.: Glyoxal vertical columns from GOME-2 backscattered light measurements and comparisons with a global model, Atmos. Chem. Phys., 10(24), 12059–12072, doi:10.5194/acp-10-12059-2010, 2010.

Lerot, C., Hendrick, F., Van Roozendael, M., Alvarado, L. M., Richter, A., De Smedt, I., Theys, N., Vlietinck, J., Yu, H., Van, J., Stavrakou, T., Müller, J.-F., Valks, P., Loyola, D., Kumar, V., Wagner, T., Schreier, S. F., Sinha, V., Wang, T., Wang, P. and Retscher, C.: Glyoxal tropospheric column retrievals from TROPOMI, multi-satellite intercomparison and ground-based validation 2 3, , doi:10.5194/amt-2021-158, n.d.

Li, J., Mao, J., Min, K.-E., Washenfelder, R. A., Brown, S. S., Kaiser, J., Keutsch, F. N., Volkamer, R., Wolfe, G. M., Hanisco, T. F., Pollack, I. B., Ryerson, T. B., Graus, M., Gilman, J. B., Lerner, B. M., Warneke, C., de Gouw, J. A., Middlebrook, A. M., Liao, J., Welti, A., Henderson, B. H., McNeill, V. F., Hall, S. R., Ullmann, K., Donner, L. J., Paulot, F. and Horowitz, L. W.: Observational constraints on glyoxal production from isoprene oxidation and its contribution to organic aerosol over the Southeast United States, J. Geophys. Res. Atmos., 121(16), 9849–9861, doi:10.1002/2016JD025331, 2016.

Liu, Z., Wang, Y., Vrekoussis, M., Richter, A., Wittrock, F., Burrows, J. P., Shao, M., Chang, C.-C., Liu, S.-C., Wang, H. and Chen, C.: Exploring the missing source of glyoxal (CHOCHO) over China, Geophys. Res. Lett., 39(10), L10812, doi:10.1029/2012GL051645, 2012.

Lorente, A., Folkert Boersma, K., Yu, H., Dörner, S., Hilboll, A., Richter, A., Liu, M., Lamsal, L. N., Barkley, M., De Smedt, I., Van Roozendael, M., Wang, Y., Wagner, T., Beirle, S., Lin, J. T., Krotkov, N., Stammes, P., Wang, P., Eskes, H. J. and Krol, M.: Structural uncertainty in air mass factor calculation for NO2 and HCHO satellite retrievals, Atmos. Meas. Tech., 10(3), 759–782, doi:10.5194/amt-10-759-2017, 2017.

Lorente, A., Folkert Boersma, K., Stammes, P., Gijsbert Tilstra, L., Richter, A., Yu, H., Kharbouche, S. and Muller, J. P.: The importance of surface reflectance anisotropy for cloud and NO2 retrievals from GOME-2 and OMI, Atmos. Meas. Tech., 11(7), 4509–4529, doi:10.5194/amt-11-4509-2018, 2018.

Loyola, D. G., Xu, J., Heue, K.-P. and Zimmer, W.: Applying FP_ILM to the retrieval of geometry-dependent effective Lambertian equivalent reflectivity (GE_LER) to account for BRDF effects on UVN satellite measurements of trace gases, clouds and aerosols, Atmos. Meas. Tech. Discuss., 1–28, doi:10.5194/amt-2019-37, 2019.

Martin, R. V.: An improved retrieval of tropospheric nitrogen dioxide from GOME, J. Geophys. Res., 107(D20), 4437, doi:10.1029/2001JD001027, 2002.

Mason, J. D., Cone, M. T. and Fry, E. S.: Ultraviolet (250–550 nm) absorption spectrum of pure water, Appl. Opt., 55(25), 7163, doi:10.1364/AO.55.007163, 2016.

Müller, J.-F. and Brasseur, G.: IMAGES: A three-dimensional chemical transport model of the global troposphere, J. Geophys. Res., 100(D8), 16445, doi:10.1029/94JD03254, 1995.

Müller, J.-F., Stavrakou, T., Bauwens, M., Compernolle, S. and Peeters, J.: Chemistry and deposition in the

Model of Atmospheric composition at Global and Regional scales using Inversion Techniques for Trace gas Emissions (MAGRITTE v1.0). Part B. Dry deposition, Geosci. Model Dev. Discuss., 1–49, doi:10.5194/gmd-2018-317, 2018.

Müller, J.-F., Stavrakou, T. and Peeters, J.: Chemistry and deposition in the Model of Atmospheric composition at Global and Regional scales using Inversion Techniques for Trace gas Emissions (MAGRITTE v1.1) – Part 1: Chemical mechanism, Geosci. Model Dev., 12(6), 2307–2356, doi:10.5194/gmd-12-2307-2019, 2019.

Myriokefalitakis, S., Vrekoussis, M., Tsigaridis, K., Wittrock, F., Richter, A., Brühl, C., Volkamer, R., Burrows, J. P. and Kanakidou, M.: The influence of natural and anthropogenic secondary sources on the glyoxal global distribution, Atmos. Chem. Phys., 8(16), 4965—4981 [online] Available from: http://www.atmos-chem-phys.net/8/4965/2008/, 2008.

Noël, S., Bramstedt, K., Bovensmann, H., Gerilowski, K., Burrows, J. P., Standfuss, C., Dufour, E. and Veihelmann, B.: Quantification and mitigation of the impact of scene inhomogeneity on Sentinel-4 UVN UV-VIS retrievals, Atmos. Meas. Tech., 5(6), 1319–1331, doi:10.5194/amt-5-1319-2012, 2012.

Palmer, P. I., Jacob, D. J., Chance, K., Martin, R. V., Spurr, R. J. D., Kurosu, T. P., Bey, I., Yantosca, R., Fiore, A. and Li, Q.: Air mass factor formulation for spectroscopic measurements from satellites: Application to formaldehyde retrievals from the Global Ozone Monitoring Experiment, J. Geophys. Res. Atmos., 106(D13), 14539–14550, doi:10.1029/2000JD900772, 2001.

Platt, U. and Stutz, J.: Differential Optical Absorption Spectroscopy: Principles and Applications, Springer-Verlag., 2008.

Puķīte, J., Kühl, S., Deutschmann, T., Platt, U. and Wagner, T.: Extending differential optical absorption spectroscopy for limb measurements in the UV, Atmos. Meas. Tech., 3(3), 631–653, doi:10.5194/amt-3-631-2010, 2010.

Richter, A.: qa4ecv_no2_inhomogeneous_scenes_171221, in QA4ECV technical note, Treatment of inhomogeneous scenes., 2018.

Richter, A., Begoin, M., Hilboll, A. and Burrows, J. P.: An improved NO<sub>2</sub> retrieval for the GOME-2 satellite instrument, Atmos. Meas. Tech., 4(6), 1147–1159, doi:10.5194/amt-4-1147-2011, 2011.

Rodgers, C. D.: Inverse Methods for Atmospheric Sounding, WORLD SCIENTIFIC., 2000.

Rodgers, C. D. and Connor, B. J.: Intercomparison of remote sounding instruments, J. Geophys. Res. D Atmos., 108(3), doi:10.1029/2002jd002299, 2003.

Van Roozendael, M., Loyola, D., Spurr, R., Balis, D., Lambert, J.-C., Livschitz, Y., Valks, P., Ruppert, T., Kenter, P., Fayt, C. and Zehner, C.: Ten years of GOME/ERS-2 total ozone data—The new GOME data processor (GDP) version 4: 1. Algorithm description, J. Geophys. Res., 111(D14), D14311, doi:10.1029/2005JD006375, 2006.

Rothman, L. S., Gordon, I. E., Babikov, Y., Barbe, A., Chris Benner, D., Bernath, P. F., Birk, M., Bizzocchi, L., Boudon, V., Brown, L. R., Campargue, A., Chance, K., Cohen, E. A., Coudert, L. H., Devi, V. M., Drouin, B. J., Fayt, A., Flaud, J. M., Gamache, R. R., Harrison, J. J., Hartmann, J. M., Hill, C., Hodges, J. T., Jacquemart, D., Jolly, A., Lamouroux, J., Le Roy, R. J., Li, G., Long, D. A., Lyulin, O. M., Mackie, C. J., Massie, S. T., Mikhailenko, S., Müller, H. S. P., Naumenko, O. V., Nikitin, A. V., Orphal, J., Perevalov, V., Perrin, A., Polovtseva, E. R., Richard, C., Smith, M. A. H., Starikova, E., Sung, K., Tashkun, S., Tennyson, J., Toon, G. C., Tyuterev, V. G. and Wagner, G.: The HITRAN2012 molecular spectroscopic database, J. Quant. Spectrosc. Radiat. Transf., 130, 4–50, doi:10.1016/j.jqsrt.2013.07.002, 2013.

Rozanov, A., Rozanov, V., Buchwitz, M., Kokhanovsky, A. and Burrows, J. P.: SCIATRAN 2.0 - A new radiative transfer model for geophysical applications in the 175-2400 nm spectral region, in Advances in Space Research, vol. 36, pp. 1015–1019, Elsevier Ltd., 2005.

Schönhardt, A., Begoin, M., Richter, A., Wittrock, F., Kaleschke, L., Gómez Martín, J. C. and Burrows, J. P.: Simultaneous satellite observations of IO and BrO over Antarctica, Atmos. Chem. Phys., 12(14), 6565–6580, doi:10.5194/acp-12-6565-2012, 2012.

Serdyuchenko, A., Gorshelev, V., Weber, M., Chehade, W. and Burrows, J. P.: High spectral resolution ozone absorption cross-sections &ndash; Part 2: Temperature dependence, Atmos. Meas. Tech., 7(2), 625–636, doi:10.5194/amt-7-625-2014, 2014.

Sinreich, R., Coburn, S., Dix, B. and Volkamer, R.: Ship-based detection of glyoxal over the remote tropical Pacific Ocean, Atmos. Chem. Phys., 10(23), 11359–11371, doi:10.5194/acp-10-11359-2010, 2010.

De Smedt, I., Müller, J.-F., Stavrakou, T., van der A, R., Eskes, H. and Van Roozendael, M.: Twelve years of global observations of formaldehyde in the troposphere using GOME and SCIAMACHY sensors, Atmos. Chem. Phys., 8(16), 4947–4963 [online] Available from: http://www.atmos-chem-phys.net/8/4947/2008/, 2008.

De Smedt, I., Stavrakou, T., Hendrick, F., Danckaert, T., Vlemmix, T., Pinardi, G., Theys, N., Lerot, C., Gielen, C., Vigouroux, C., Hermans, C., Fayt, C., Veefkind, P., Müller, J.-F. and Van Roozendael, M.: Diurnal, seasonal and long-term variations of global formaldehyde columns inferred from combined OMI and GOME-2 observations, Atmos. Chem. Phys., 15(21), 12519–12545, doi:10.5194/acp-15-12519-2015, 2015.

Spurr, R. and Christi, M.: The LIDORT and VLIDORT Linearized Scalar and Vector Discrete Ordinate Radiative Transfer Models: Updates in the Last 10 Years, pp. 1–62, Springer, Cham., 2019.

Stavrakou, T., MÃ¼ller, J.-F., De Smedt, I., Van Roozendael, M., Kanakidou, M., Vrekoussis, M., Wittrock, F., Richter, A. and Burrows, J. P.: The continental source of glyoxal estimated by the synergistic use of spaceborne measurements and inverse modelling, Atmos. Chem. Phys., 9(21), 8431–8446 [online] Available from: http://www.atmos-chem-phys.net/9/8431/2009/, 2009.

Stavrakou, T., Müller, J.-F., Boersma, K. F., van der A, R. J., Kurokawa, J., Ohara, T. and Zhang, Q.: Key chemical NO_x sink uncertainties and how they influence top-down emissions of nitrogen oxides, Atmos. Chem. Phys., 13(17), 9057–9082, doi:10.5194/acp-13-9057-2013, 2013.

Stavrakou, T., Müller, J.-F., Bauwens, M., Smedt, I. De, Lerot, C., Roozendael, M. Van, Coheur, P.-F., Clerbaux, C., Boersma, K. F., A, R. van der, Song, Y., Jeong, S.-J., Huang, X., Song, Y., Li, M., Li, J., Zhu, T., Yamaji, K., Werf, G. R. van der, Huang, X., Li, M., Li, J., Song, Y., Fu, T.-M., Levelt, P. F., Smedt, I. De, Smedt, I. De, Boersma, K. F., Lerot, C., Müller, J.-F., Stavrakou, T., Stavrakou, T., Müller, J.-F., Smedt, I. De, Roozendael, M. Van, Werf, G. van der, Giglio, L., Guenther, A., Stavrakou, T., Guenther, A., Karl, T., Harley, P., Wiedinmyer, C., Palmer, P. I., Geron, C., Li, M., Andreae, M. O., Merlet, P., Akagi, S., Kurokawa, J., Sun, L., Jin, X., Holloway, T., Safieddine, S., Chaudhry, Z., Shi, Z., Tao, J. Z., Wang, Z., Han, D., Li, S., Su, L., Chen, L., Deng, X., Dee, D. P., Randerson, J., Chen, Y., Werf, G., Rogers, B., Morton, D., Kaiser, J., Wiedinmyer, C., Kudo, S., Inomata, S., Warneke, C., Yokelson, R. J., Korontzi, S., McCarty, J., Loboda, T., Kumar, S., Justice, C., Fu, T.-M., Stavrakou, T., Castellanos, P., Boersma, K. F., Werf, G. R. van der, Razavi, A., Stavrakou, T., Lin, J., Castellanos, P., Boersma, K. F., Torres, O., Haan, J. F. de, Barkley, M. P., Roberts, G., Wooster, M. J., Lagoudakis, E., Stavrakou, T., Miller, C. C., Jacob, D. J., et al.: Substantial Underestimation of Post-Harvest Burning Emissions in the North China Plain Revealed by Multi-Species Space Observations, Sci. Reports, Publ. online 31 August 2016; | doi10.1038/srep32307, 6, 615–619, doi:10.1038/SREP32307, 2016.

Thalman, R. and Volkamer, R.: Temperature dependent absorption cross-sections of O2–O2 collision pairs between 340 and 630 nm and at atmospherically relevant pressure, Phys. Chem. Chem. Phys., 15(37), 15371, doi:10.1039/c3cp50968k, 2013.

Vandaele, A. C., Hermans, C., Simon, P. C., Carleer, M., Colin, R., Fally, S., Mérienne, M. F., Jenouvrier, A. and Coquart, B.: Measurements of the NO2 absorption cross-section from 42 000 cm−1 to 10 000 cm−1 (238–1000 nm) at 220 K and 294 K, J. Quant. Spectrosc. Radiat. Transf., 59(3–5), 171–184, doi:10.1016/S0022-4073(97)00168-4, 1998.

Veefkind, J. P., Aben, I., McMullan, K., Förster, H., de Vries, J., Otter, G., Claas, J., Eskes, H. J., de Haan, J. F., Kleipool, Q., van Weele, M., Hasekamp, O., Hoogeveen, R., Landgraf, J., Snel, R., Tol, P., Ingmann, P., Voors, R., Kruizinga, B., Vink, R., Visser, H. and Levelt, P. F.: TROPOMI on the ESA Sentinel-5 Precursor: A GMES mission for global observations of the atmospheric composition for climate, air quality and ozone layer applications, Remote Sens. Environ., 120, 70–83, doi:10.1016/j.rse.2011.09.027, 2012.

Vigouroux, C., Langerock, B., Bauer Aquino, C. A., Blumenstock, T., Cheng, Z., De Mazière, M., De Smedt, I., Grutter, M., Hannigan, J. W., Jones, N., Kivi, R., Loyola, D., Lutsch, E., Mahieu, E., Makarova, M., Metzger, J.-M., Morino, I., Murata, I., Nagahama, T., Notholt, J., Ortega, I., Palm, M., Pinardi, G., Röhling, A., Smale, D., Stremme, W., Strong, K., Sussmann, R., Té, Y., van Roozendael, M., Wang, P. and Winkler, H.: TROPOMI–Sentinel-5 Precursor formaldehyde validation using an extensive network of ground-based Fourier-transform infrared stations, Atmos. Meas. Tech., 13(7), 3751–3767, doi:10.5194/amt-13-3751-2020, 2020.

Volkamer, R., Spietz, P., Burrows, J. and Platt, U.: High-resolution absorption cross-section of glyoxal in the

UV—vis and IR spectral ranges, J. Photochem. Photobiol. A Chem., 172(1), 35—46 [online] Available from: http://www.colorado.edu/chemistry/volkamer/publications/articles/Volkamer etal (2005) HR cross section glyoxal.pdf, 2005.

Volkamer, R., Baidar, S., Campos, T. L., Coburn, S., DiGangi, J. P., Dix, B., Eloranta, E. W., Koenig, T. K., Morley, B., Ortega, I., Pierce, B. R., Reeves, M., Sinreich, R., Wang, S., Zondlo, M. A. and Romashkin, P. A.: Aircraft measurements of BrO, IO, glyoxal, NO2, H2O, O2–O2 and aerosol extinction profiles in the tropics: comparison with aircraft-/ship-based in situ and lidar measurements, Atmos. Meas. Tech., 8(5), 2121–2148, doi:10.5194/amt-8-2121-2015, 2015.

Voors, R., Dobber, M., Dirksen, R. and Levelt, P.: Method of calibration to correct for cloud-induced wavelength shifts in the Aura satellite's Ozone Monitoring Instrument, Appl. Opt., 45(15), 3652–3658, doi:10.1364/AO.45.003652, 2006.

Vrekoussis, M., Wittrock, F., Richter, A. and Burrows, J. P.: Temporal and spatial variability of glyoxal as observed from space, Atmos. Chem. Phys., 9(13), 4485–4504, doi:10.5194/acp-9-4485-2009, 2009.

Vrekoussis, M., Wittrock, F., Richter, A. and Burrows, J. P.: GOME-2 observations of oxygenated VOCs: what can we learn from the ratio glyoxal to formaldehyde on a global scale?, Atmos. Chem. Phys., 10(21), 10145–10160, doi:10.5194/acp-10-10145-2010, 2010.

Wang, Y., Tao, J., Cheng, L., Yu, C., Wang, Z., Chen, L., Wang, Y., Tao, J., Cheng, L., Yu, C., Wang, Z. and Chen, L.: A Retrieval of Glyoxal from OMI over China: Investigation of the Effects of Tropospheric NO2, Remote Sens., 11(2), 137, doi:10.3390/rs11020137, 2019.

Washenfelder, R. A., Young, C. J., Brown, S. S., Angevine, W. M., Atlas, E. L., Blake, D. R., Bon, D. M., Cubison, M. J., de Gouw, J. A., Dusanter, S., Flynn, J., Gilman, J. B., Graus, M., Griffith, S., Grossberg, N., Hayes, P. L., Jimenez, J. L., Kuster, W. C., Lefer, B. L., Pollack, I. B., Ryerson, T. B., Stark, H., Stevens, P. S. and Trainer, M. K.: The glyoxal budget and its contribution to organic aerosol for Los Angeles, California, during CalNex 2010, J. Geophys. Res., 116(D21), D00V02, doi:10.1029/2011JD016314, 2011.

Wittrock, F., Richter, A., Oetjen, H., Burrows, J. P., Kanakidou, M., Myriokefalitakis, S., Volkamer, R., Beirle, S., Platt, U. and Wagner, T.: Simultaneous global observations of glyoxal and formaldehyde from space, Geophys. Res. Lett., 33(16), L16804, doi:10.1029/2006GL026310, 2006.

Zhou, Y., Brunner, D., Boersma, K. F., Dirksen, R. and Wang, P.: An improved tropospheric NO $_2$ retrieval for OMI observations in the vicinity of mountainous terrain, Atmos. Meas. Tech., 2(2), 401–416, doi:10.5194/amt-2-401-2009, 2009.

A. Description of prototype software

The prototype algorithm for the retrieval of glyoxal slant columns is developed using the QDOAS software, a multi-purpose DOAS analysis software developed at BIRA-IASB since early nineties.

The QDOAS fitting algorithm uses a combination of Singular Value Decomposition (SVD) and the Levenberg-Marquard methods to solve the linear and non-linear parts of the DOAS equation (Danckaert et al., 2017).

The main QDOAS features include:

- Analysis
    - DOAS/intensity fitting modes;
    - shift/stretch fully configurable for any spectral item (cross-section or spectrum);
    - possibility to filter spectra and cross-sections before analysis (supported filters include Kaiser, gaussian, boxcar, Savitsky Golay…);
    - possibility to define gaps within fitting intervals (e.g. to eliminate bad pixels);
    - possibility to fit an instrumental offset;
    - possibility to define several configurations of spectral windows under a project;
    - non-linear parameters (offset, shift and stretch) can be fitted using wavelength polynomials up to the second order.
- Calibration and slit function characterization
    - wavelength calibration and instrumental slit function characterization using a non-linear least-squares (NLLS) fitting approach where measured intensities are fitted to a high resolution solar spectrum degraded to the resolution of the instrument. The fitting method (DOAS or intensity fitting) can be different from the method used in the analysis;
    - possibility to correct for atmospheric absorption and Ring effect;
    - supports different analytical line shapes.
- Cross-sections handling
    - possibility to calculate differential absorption cross-sections (by orthogonalization or high-pass filtering);
    - possibility to correct cross-sections using wavelength dependent AMF;
    - possibility to fix the column density of any selected species;
    - possibility to convolve cross-sections in real time using a user defined slit function or the information on calibration and slit function provided by the wavelength calibration procedure;
    - possibility to handle differences in resolutions between measured and control spectra;
    - standard and I_0-corrected convolutions are supported;
    - calculates Ring effect cross-sections (Rotational Raman Scattering approach);

QDOAS has been developed in collaboration with the Dutch company S[&]T. The graphical user interface is built on the Open-Source version of the QT-4 toolkit, a cross-platform application framework, and QWT libraries. QDOAS is a free software distributed under the terms of the GNU General Public License; it is open source and the code is available on request by contacting authors.

Errors on slant column densities in QDOAS

The slant column density is fitted linearly according to Equation (6-7). Uncertainties on the retrieved slant columns N_s depend on the sensitivity of the sum of squares (6-7) with respect to variations of the slant column around the fitted minimum and on the measurement noise. We use the following expression for the covariance matrix Σ of the weighted linear least squares parameter estimate:

$$\Sigma = (J^T \mathrm{E}^2 J)^{-1} \qquad \text{A-1}$$

where the matrix $J(j \times k)$ is formed by the absorption cross-sections, and the diagonal matrix $E(k \times k)$ contains the measurement errors (with k the number of spectral pixels in the fitting interval):

$$\mathrm{E}_{ij} = \frac{1}{\varepsilon_i} \quad if\ i = j \qquad \text{A-2}$$

If the measurement errors ε_i are not used in the fit (baseline), all ε_i are set to 1 and the random error on the measurements ε^2 is estimated by the reduced χ^2, e.g. the sum of squares (6-7) divided by the number of degrees of freedom in the fit (k-n), where n is the number of fitted parameters. Equation (A-1) then becomes:

$$\Sigma = \frac{\chi^2}{(k-n)} (J^T J)^{-1} \qquad \text{A-3}$$

The diagonal elements of this matrix define the slant column random error $\sigma_{N,s,j}$ for each absorber j included in the DOAS fit:

$$\sigma^2_{N,s,j} = \frac{\chi^2}{(k-n)} (J^T J)^{-1} \Big)_{j,j} \qquad \text{A-4}$$

This estimate for the uncertainties assumes that the errors on the measurements at each spectral pixel are independent and normally distributed. When measurement errors are correlated or contain systematic components, the uncertainties calculated with (A-1) will underestimate the true error on the slant column density. Remaining residual structures after the fit, or a value of $\frac{\chi^2}{(k-n)} \gg 1$, are an indication of such a bad fit.

Equations (A-1) or (A-3) do not take into account the uncertainties on the cross sections, or other systematic errors in the fit parameters.

B. Averaging kernels

Retrieved satellite quantities always represent a weighted average over all parts of the atmosphere that contribute to the signal observed by the satellite instrument. The DOAS total column retrieval is implicitly dependent on the a priori gas profile n_a. Indeed, the radiative transfer calculation accounts for the sensitivity of the measurement to the CHOCHO concentrations at all altitudes and the sensitivities are weighted with the assumed a priori profile shape to produce the vertical column. The averaging kernel (A) is proportional to this measurement sensitivity profile, and provides the relation between the retrieved column N_v and the true tracer profile x (Rodgers, 2000; Rodgers and Connor, 2003):

$$N_v - N_{v,a} = A.(x^{pc} - n_a^{pc}) \tag{B-1}$$

where the profiles are expressed in partial columns (*pc*). For total column observations of optically thin absorbers, DOAS averaging kernels are calculated as follows (Eskes and Boersma, 2003): $A(z) = \frac{m(z)}{M}$, where $m(z)$ is the altitude-resolved air mass factor and M is the tropospheric air mass factor (calculated from equation 6-10). The air mass factor, and therefore the retrieved vertical column, depends on the a priori profile shape, in contrast to the altitude-resolved air mass factor which describes the sensitivity of the slant column to changes in trace gas concentrations at a given altitude and does not depend on the a priori profile in an optically thin atmosphere. From the definition of A, we have $N_{v,a} = A.n_a^{pc}$ and Equation (B-1) simplifies to:

$$N_v = A.x^{pc} \tag{B-2}$$

The averaging kernel varies with the observation conditions. In the CHOCHO retrieval product, the AK is provided together with the error budget for each individual pixel. The provided CHOCHO vertical columns can be used in two ways, each with its own associated error (Boersma et al., 2004):

1. For independent study and/or comparison with other independent measurements of total column amounts. In this case, the total error related to the column consists of slant column measurement errors, reference sector correction errors, and air mass factor errors. The latter consists of errors related to uncertainties in the assumed profile $n_a$and errors related to the $m(z)$ parameters as developed in section 6.5.
2. For comparisons with chemistry transport models or validation with independent profile measurements, if the averaging kernel information is used, the a priori profile shape error no longer contributes to the total error. Indeed, the relative difference between the retrieved column N_v and an independent profile x_i is:

$$\delta = \frac{N_v - A.x_i^{pc}}{N_v} \tag{B-3}$$

The total AMF M cancels since it appears as the denominator of both N_v and A. Because only the total AMF depends on the a priori tracer profile n_a, the comparison using the averaging kernel is not influenced by the chosen a priori profile shape. The a priori profile error does not influence the comparison, but of course, it still does influence the error on the retrieved vertical column.